Internet of Things 31 (2025) 101571

Contents lists available at ScienceDirect

Internet of Things

journal homepage: www.sciencedirect.com/journal/internet-of-things

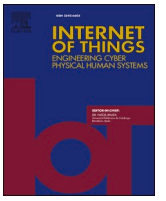

AI-driven insights into B5G/6G MAC mechanisms: A comprehensive analysis

Djamila Talbi *, Zoltan Gal

Faculty of Informatics, University of Debrecen, Debrecen, Hungary

ARTICLE INFO

Keywords:
B5G/6G
Medium access control
Entropy
Artificial intelligence

ABSTRACT

In the 6G wireless communication domain, optimizing the medium access control mechanism is crucial for enhancing the performance of high-speed, over Terabit/sec transmission rate networks. This paper evaluates the adaptive directional antenna protocol for terahertz frequencies technology using the ns-3 simulator, employing different techniques like Shannon entropy, wavelet transform, supervised, unsupervised machine learning, and classical processing methods focusing on the impact of the two used parameters: overlapping ratio and the rotation step. Our approach is to highlight the importance of the *Paleo-AI Classical Processing* method, which is about incorporating the classical mathematical processing method, with the AI models for better results. The proposed method includes applying some analytical tools like the entropy metrics to understand the dynamic behavior of the radio control frames, particularly in distinguishing between the stable and unstable phases of the communication process and includes the adoption of fractal wavelet analysis for better learning. Additionally, the RNN classification of MAC event sequences into categories supported by transfer learning enhanced the model's efficiency, where we introduced the weighted accuracy to time ratio, a novel approach to assess the competency of various deep learning models. Moreover, different generative AI methods were used to produce synthetic data where the similarity levels were quantified by using six distinct metrics. The overall results of this paper demonstrated the necessity of adapting the MAC protocols to specific environmental conditions, thereby contributing to the development of more resilient B5G/6G communication networks.

1. Introduction

Beyond 5th Generation (B5G) and 6th Generation (6G) wireless networks are still in their early stage, promising to bring high-speed internet connection with 1 Tbps speed, new technologies and services appear. The key to this evolution is the exploration of Terahertz (THz) frequencies which are essential to achieve ultra-high security, energy efficiency, and low latency. These high frequencies offer vast potential to handle ultra-dense networks and open the opportunity for new applications that require high precision and minimal latency to emerge. Reaching these ambitious goals poses considerable challenges such as molecular absorption losses which require advanced solutions concerning the overall system including channel modeling, antenna design, and signal processing.

In parallel, Incorporating Artificial Intelligence (AI) into such new wireless technology is poised to unlock new services and facilitate the application of the technology, ensuring that it will not only be faster but also smarter and more resilient. AI allows the

* Corresponding author.
E-mail address: talbi.djamila@inf.unideb.hu (D. Talbi).

https://doi.org/10.1016/j.iot.2025.101571

Available online 11 March 2025

List of Symbols used in the paper

Symbols	*Meaning*
a	Threshold
A	Area of circle
$\boldsymbol{A_i}$	Area of sector
C	Classes
d	Topology type
f	Feature vector
L	Packet size
$\boldsymbol{m}$	Overlapping ratio
$\boldsymbol{m}_0$	slope
M	Inte-subsystem mutual effect
n	Number of MTs
N	Number of sectors
P	Received power
p	Probability
r	Cell radius
R	Relative entropy difference
$\boldsymbol{R_{Tx}}$	Transmission rate
s	Rotation step
S	Entropy
$\boldsymbol{t_{sec}}$	Sector time
$\boldsymbol{t_{sim}}$	Simulation time
T	Taught layer
U	Untaught layer
V	MTs number set
$\boldsymbol{\alpha}$	Weight
$\boldsymbol{\delta}$	Sequence vector
$\boldsymbol{\eta}$	Entropy ratio
$\boldsymbol{\varphi}$	Angle of the sector

network to self-optimize in real-time based on varying conditions, managing the enormous amount of data generated and making the network more robust against cyber-attacks. Wavelet transform is considered a powerful mathematical tool for signal processing, feature extraction, and data compression. It can be integrated with AI and deep learning algorithms to enhance and speed up the learning process. Moving to information theory, an essential aspect in developing the next wireless communication technology, Shannon Entropy helps quantify the amount of uncertainty or information content in a system for an efficient design and optimized system. Applying Shannon entropy helps with data compression, security protocols, and channel coding. Therefore, it is among the aspects that should be considered to overcome 6G's objections. Shannon entropy can be also utilized in AI-driven networks for decision-making optimization processes affirming that the most valuable data is prioritized in network operations.

Traditional data processing methods and mathematical tools alone are often insufficient for effectively handling and treating the data sets. They typically rely on formulas and assumptions that limit their adaptability. We also tend to believe that directly applying modern AI techniques to raw data sets is not optimal due to high computational costs and complexity. Instead, we propose a hybrid approach, the *Paleo-AI Classical Processing* (PACP) method, where traditional mathematical tools are first used to preprocess and enhance data visibility, preparing it for targeted AI-based training and classification. This combined method reduces the cost and complexity of the used AI and maximizes data quality, improving overall efficiency and performance. On the topic of the high-speed communication network B5G/6G, in this paper, our primary contribution is to demonstrate the significance of the PACP method on THz-based data, showing how this approach enhances AI model performance and adaptability. We aim to validate that the PACP method optimizes data for AI processing and holds potential for real-world applications, enabling enhanced, cost-effective AI solutions in THz communication scenarios. The integration of different PACP methods using different machine learning techniques is highlighted in this paper and shown in the Fig. 1. Diverse types of MAC protocol analysis using numerous approaches, while some of them are as follows:

- An interpretation of the MAC pre-standard's basic mechanism called Adaptive Directional Antenna Protocol for Terahertz (ADAPT) [33] (Fig. 1, block ID: 0). Along with a comprehensive analysis of the properties of the simulation data, focusing on the core principles and processes that guide its functionality. Additionally, it encompasses a thorough examination of the characteristics of the ns-3 simulation data, that are crucial for showing and understanding the pre-standard performances in various scenarios and environments.

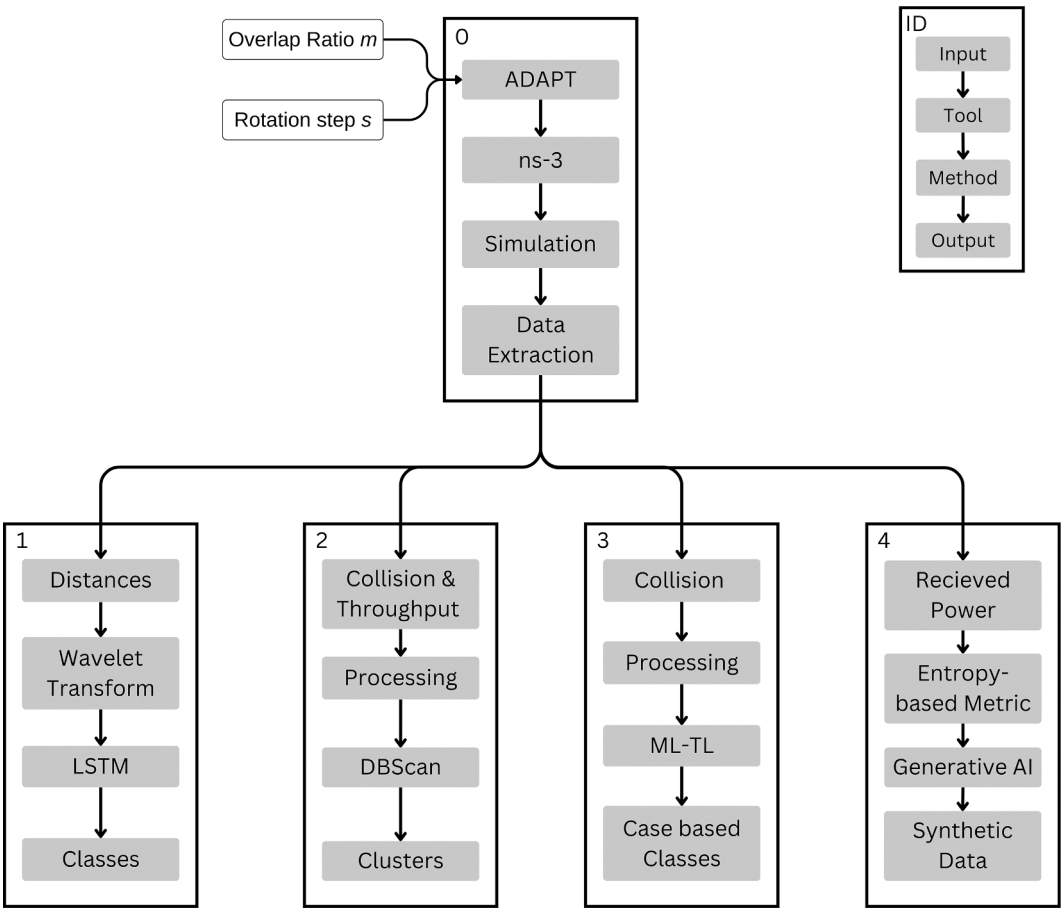

Fig. 1. Schematic diagram of the data analysis flow.

- Integration of two parameters to the ADAPT protocol for enhancing the communication opportunities, by optimizing network interactions. These parameters allow for improving the alignment and adaptability in signal transmission, boosting the connection opportunities, the integration is shown in Fig.1, block ID: 0.
- Wavelet transform was applied to the data (Fig. 1, block ID: 1) for feature extraction. It enables us to capture both transient and persistent characteristics over time. This method prepares the data for the training using a neural network, enhancing the model's ability to learn complex patterns, and improving its overall performance in classification tasks.
- Throughput and collision data were treated, forming the so-called sector efficiency data set. After that, an unsupervised machine learning clustering method was executed to identify patterns and relationships within the data (Fig. 1, block ID: 2). This approach allows us to uncover the hidden structures and optimize resource allocation across different sectors.
- ADAPT-based collision data sets were also processed to prepare them for the AI phase of multi-layer transfer learning (ML-TL) (Fig. 1, block ID: 3). A novel metric was proposed to quantify the effectiveness of the AI model, allowing for more accurate assessment of its performance and facilitating comparisons between different models.
- Shannon Entropy was examined to study the mobile terminals' mutual effect (Fig. 1, block ID: 4). It provides insights into the variability and distribution of communication patterns among users. By quantifying the uncertainty in these interactions, we can pinpoint factors affecting performance and inform strategies for optimizing overall network system.
- The paper thoroughly discusses the application of PACP, which incorporates four different artificial intelligence techniques alongside classical processing methods across various simulation scenarios. It also details the properties of the B5G/6G-based ADAPT medium access mechanism and introduces several metrics for evaluation.

To facilitate comprehension and coherence, this paper is organized into distinct sections. The second section presents an extensive review of existing literature, emphasizing recent enhancements in the field, and underscoring recent advancements and trends in the field, while critically analyzing prior research contributions. In section three, we outline the methodology used for simulation and analysis, with a specific focus on the MAC mechanism. This section explains used simulation tools, data extraction methodology, parameters, experimental steps, and analytical techniques utilized in our study. Section four delves into various artificial intelligence approaches, exploring their specific contributions to the research and assessing their effectiveness in addressing the challenges posed

by the MAC mechanism. Finally, the concluding section synthesizes our key findings, reflecting on their implications for the field, and process potential avenues for future research, encouraging further exploration of innovative solutions to enhance communication technologies.

2. Related work

Given the broad scope of the research topic addressed in this paper, which encompasses a variety of interconnected studies and disciplines. We organize our examination of the related work into distinct sections. This approach allows us to systematically explore the relevant literature, ensuring that we adequately cover the various aspects of our topic. By segmenting the related work into three main parts, we aim to provide a clearer understanding of how each part contributes to the overall framework of our research.

2.1. Medium access mechanisms in 6G networks

The field of high-speed wireless networks using machine learning has garnered significant attention over the past decade. This section will give a brief talk about the most relevant studies, highlighting their contributions and the objectives of this research. Developing the next generation of wireless communication requires several efforts due to the new frequency band that will operate on, therefore researchers in [1] propose to use a new IP architecture having new Quality of Service (QoS) aspects, integrating Machine Learning (ML) along with 6G technology enhance the service efficiency and help to meet its requirements [2]. In addition, the authors in [3] propose to use a receiver-initiated handshake for ensuring the synchronization in the THz communication channel, however moving to new frequencies causes new challenges, therefore, a transceiver architecture having ultra-broadband and multi-band was suggested in [4] to overcome the objections, while in [5] a wireless link called Single Input Single Output (SISO) is proposed to reach 100 Gbit/s data rate. The growth of internet use and technology requires network infrastructure, based on the QoS of the 5G networks, an enhanced cat swarm optimization (ECSO) was proposed for optimization purposes [6]. The applied method increases the throughput by 8 % and shortens response time by 7 % compared to the existing algorithms. This study would underscore the importance of maintaining user experience in dense and high-demand settings in the 6G wireless communication network.

The importance of developing terahertz communication lies in its potential to achieve data rates over 100 Gbps and latency under 1 millisecond for 6G systems [7]. This technology supports applications such as Tera-WIFI and THz wireless backhaul, and advancement in THz technologies is pivotal in bridging the THz GAP, positioning terahertz communication as a foundational element of future wireless systems. Nevertheless, developing a suitable MAC protocol for terahertz communication is essential to address challenges such as high path loss and scattering, which restrict communication distances [8]. As a solution for the bandwidth demands of the 6G technology, it introduced full-spectrum wireless communication (FSWC) [9], that utilizes the entire electromagnetic spectrum, from microwaves to ultraviolet light, addressing the spectrum shortage and enabling a new communication paradigm.

2.2. Shannon entropy in wireless networks

Nevertheless, the application of Shannon entropy in wireless communication and sensor networks has emerged as a crucial field, being a crucial decision metric, reducing energy consumption [10]. Moreover, the idea of enhancing the corona IPv6 routing protocol for low-power and lossy networks (CoRPL) [10] routing protocol by integrating the mobility entropy helps in reducing the packet loss and optimizing the used power [11], meanwhile, the entropy was used for the same purpose in [12]. In the IoT domain, Shannon entropy plays an important role in enhancing the feature selection for wireless signal processing and for small electronics [13] and helps in increasing the significance of harnessing energy from environmental sources [14]. Shannon entropy was used for other aims in wireless communication technologies and meshed with some applications due to its capability in the information theory field, showing its strength in optimizing data transmission, encoding, and compression techniques [15–17]. Moreover, research was made to explore the transport capacity of multi-node wireless networks through information theory, considering how distance and signal attenuation impact information transfer [18]. Information-theoretic principles reveal that cooperation between nodes and multiuser estimation can significantly improve capacity under favorable conditions.

Topological entropy was used to analyze wireless networks affected by scattering and shadowing [19]. New entropy bounds are derived based on fading distributions, showing that different models lead to distinct network entropies. In the AI field, Shannon entropy was explored as a key tool in information theory [20], particularly in measuring uncertainty for efficient data transfer, compression, and classification. Results show that higher entropy reflects greater system uncertainty. Entropy also proved that it could minimize bit usage in data coding, aiding effective communication and storage. Overall, the study underscores entropy's foundational role in AI, big data, and deep learning, inspiring new approaches to uncertainty measurement across disciplines.

2.3. Usage of artificial intelligence in 6G network

Moving to Transfer Learning (TL) ML, where it is considered, a powerful tool enabling models to leverage knowledge from related tasks or domains to improve performance on a target task. Multi-layer TL allows more sophisticated knowledge to transfer across multiple layers of the neural networks. As said, a Long-Short Term Memory (LSTM) multilayer RNN was implemented to achieve 87.94 % learning accuracy [21], and authors [22] reached 97 % accuracy using different prediction models.

To reduce the computational complexity and minimize the training overhead that most of the ML suffers from, the researchers in [23] present an enhanced algorithm, learned-sparse Bayesian learning with generalized approximate message passing (L-SBL-GAMP)

for designing hybrid precoders and combiners in mmWave massive MIMO systems. While the simulation achieves a higher rate and improved accuracy in large-scale MIMO systems.

For achieving high accuracy, the researchers in [24–26] highly recommend using a pre-trained model for transfer learning besides pre-processing using augmentation and segmentation in addition to hybrid convolutional. Recurrent NN exhibits excellent performance by using Bi-Directional Long-Short Term Memory (BiLSTM) with 92.05 % testing accuracy [27], this high level of accuracy proves the effectiveness of the used model in capturing forward and backward dependencies in sequential data. Artificial Neural Network (ANN) was used on real-world data collected through dive tests in [28], it examines the relationship between QoS parameters and user satisfaction for various multimedia services. The ANN model simulates the user experience producing a quality of experience (QoE) score that informs network optimization, offering a practical framework for mobile network operators to improve service quality aligned with user satisfaction. The ANN was also used in another study [29] to estimate QoE scores from QoS metrics, enabling a self-tuning approach in long-term evolution (LTE) networks for optimizing resource block allocation. With particle genetic efficiency algorithm (PGA) to adjust service priorities, this method improves user satisfaction and resource efficiency.

The authors in [30] propose a metric for evaluating the performance of a deep learning method known as DAWNBENCH using Time-To-Accuracy (TTA), this metric is designed to compare different DL techniques by measuring the learning time for reaching a specified accuracy level. Meanwhile, another research group [31] presents a framework for uncertainty quantification (UQ) in NNs validated through comparative studies on prototype problems. An open-source Python, NeuralUQ is developed to facilitate UQ implementation in scientific machine learning, along with tutorials and computational experiments. In the field of DL, research was done [32] to explore its role in managing vast data generated by the IoT. With billions of devices capturing diverse data, DL techniques enable anomaly detection, trend forecasting, and control for secure, efficient IoT operations. This research highlights the main opportunities that DL could give for future advancement in this field.

3. Extracting and analyzing methodology of the 6G network-based ADAPT data

In this section, we provide a detailed explanation of the extracted data set, discuss the methodologies used, conduct through analysis of the B5G/6G wireless communication network medium access control mechanism, and give a comprehensive discussion of the findings.

3.1. ADAPT MAC mechanism data extraction

We present an in-depth overview of the extracted data set, outlining its key characteristics, source, and relevance to our research objectives. We will detail the methodologies employed in the data extraction process, highlighting the steps taken to ensure data accuracy, reliability, and integrity. Following this, we conduct a thorough analysis of the MAC mechanism. This analysis will encompass a review of the MAC protocol, examining its performance metrics, efficiency, and adaptability to the unique demands of emerging communication technologies.

3.1.1. TeraSim extension overview

In this subsection, we introduce the proposed MAC mechanism by D. Morales and J. Jornet [33] with some found properties. ADAPT MAC protocol is compatible with the first standardization IEEE 802.15.3d of the physical layer for the THz frequencies [34], operates on the same frequency band that the 6G/B5G operates on, this standardization includes six modulation schemes ranging from binary (BPSK) to quadrature amplitude modulation 64 (64-QAM) which are all included in ADAPT. Moreover, it utilizes the high rate of forward error correction (FEC) (14/15) supported by IEEE 802.15.3d. The THz frequency is the way that will lead the new wireless

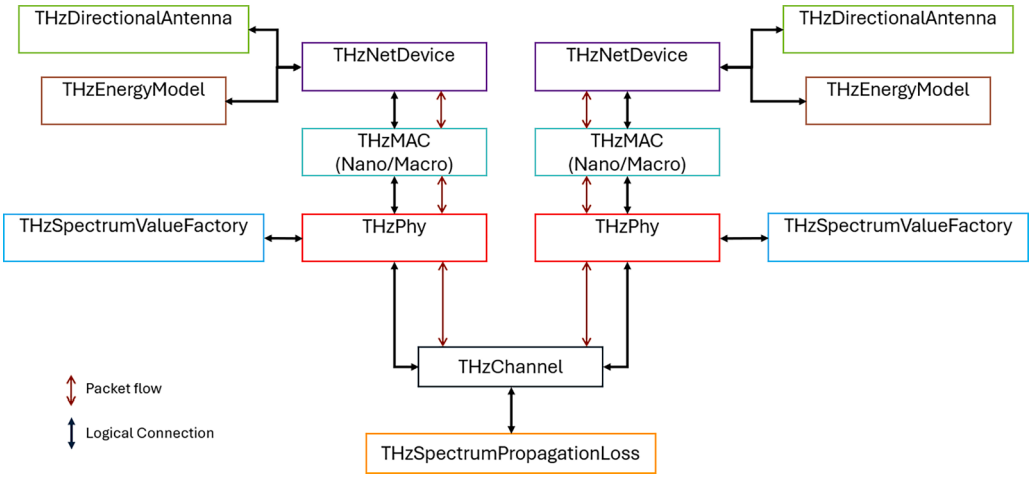

Fig. 2. The architecture of the models integrated into the TeraSim extension.

communication generation to overcome most of the challenges that it faces, and it helps it to reach its requirements. For extracting the data, we used *ns-3* to simulate the example 'macroscale scenario' provided in the TeraSim tool [35] version two.

TeraSim is an *ns-3* extension designed to model wireless communication in the THz frequency band, As the authors mentioned in [35], the unique properties of the THz band provide an enormous bandwidth ranging from tens GHz to a few THz which inspired them in the design. Besides its advantages, communication can be affected by spreading loss and molecular absorption, However, these effects become more pronounced over longer distances. Therefore, TeraSim provides two main examples; I) Nanoscale scenario: that covers shorter distances (under one meter) and the THz band can be treated as a single, wide transmission window (around 10 THz in width). II) Macroscale scenario: this provided example is mainly for longer distances, and the THz band splits into multiple, narrower transmission windows, each ten GHz wide, due to the molecular absorption. Also to overcome the high path loss, this scenario uses directional or beamforming antennas, while energy harvesting is typically not necessarily due to the larger power budget.

Both Nanoscale and Macroscale used a unified and modular architecture as shown in the Fig. 2. And explained in the pseudocode Algorithm. 1, The **THzNetDevice** in TeraSim serves as the core component of each node, functioning as the Network Interface Card (NIC) to handle both the Physical (PHY) and MAC layers. The **THzPhy** uses the **THzSpectrumValueFactory** to generate pulses for nanoscale communication and continuous carrier waveforms for macroscale scenarios. Communication between nodes is done through the **THzChannel** that uses the **THzSpectrumPropagationLoss** to calculate the effect of spreading loss and absorption on different frequency bands. For the nanoscale scenarios, energy efficiency is critical. Therefore, the **THzEnergyModel** is integrated into each node to help nanodevices maintain long-term functionality. The **THzNetDevice** also manages the antenna system; for nanoscale applications, it operates omnidirectionally, while for macroscale applications, it switches to highly directional or beamforming antennas to overcome the increased path loss. TeraSim implements two well-known MAC protocols ALOHA and Carrier Sense Multiple Access (CSMA) which are adapted to meet the specific needs of the physical layer of each scenario. The **THzDirectionalAntenna** and energy **THzEnergyModel** are specialized for nanoscale and macroscale communications, however, it can be adapted to work across

Algorithm 1
Terasim *nanoscale* and *macroscale* pseudocode.

```
                    // Initialize TeraSim Simulation
1.                  Initialize Simulation
2.                    Create ns-3 Node objects
3.                    For each Node
4.                      Create THzNetDevice
5.                      Attach THzNetDevice to Node
                    // Set up THz Channel
6.                  Create THzChannel
7.                    Set THzSpectrumPropagationLoss to calculate spreading and absorption loss
                    // Define Communication Scenarios (Nanoscale and Macroscale)
8.                  If Distance < 1 meter
                      // Nanoscale Scenario Setup
9.                    For each Node
10.                     Create THzMAC and THzPhy for Nanoscale
11.                     Set PHY to generate pulses using THzSpectrumValueFactory
12.                     Set Antenna to Omnidirectional
13.                     Attach THzEnergyModel to Node for energy harvesting
14.                     Configure MAC protocol
15.                 Else
                      // Macroscale Scenario Setup
16.                   For each Node
17.                     Create THzMAC and THzPhy for Macroscale
18.                     Set PHY to generate carrier waveform using THzSpectrumValueFactory
19.                     Set the Antenna to Directional or Beamforming mode
20.                     No energy harvesting is needed
21.                     Configure MAC protocol
                    // Configure Node Communication
22.                 For each Node
23.                   Attach THzNetDevice to Node
24.                   Set communication path via THzChannel
25.                   Calculate losses using THzSpectrumPropagationLoss
                    // Run Simulation
26.                 Start Simulation
27.                   For each communication event
28.                     If Nanoscale Scenario
29.                       Generate femtosecond pulses
30.                       Use omnidirectional antenna for transmission
31.                       Harvest energy as needed
32.                     Else
33.                       Generate carrier waveform
34.                       Use a directional antenna to focus power on transmission windows
35.                   Update MAC layer based on packet transmission success/failure
36.                 End Simulation
```

both with minor tweaks to the MAC layer. This flexibility makes TeraSim a powerful extension for ns-3 for exploring the THz band communication networks.

3.1.2. MAC ADAPT protocol

The proposed ADAPT protocol is performed in a cell with a radius of tens of meters divided into equally sized sectors as shown in Fig. 3, with the Access Point (AP) in the canter surrounded by the Mobile Terminals (MTs). We applied two distribution topology types; d1: centered distribution having the MTs distributed randomly closer to the AP, and d2: uniform distribution having the MTs distributed randomly uniform around the central point. Table 1 provides all the parameters that we used for our simulation.

To manage the access control, the ADAPT protocol used the 3-way handshake to establish the connection between the AP and the MTs (see Fig. 4). The AP starts to send a *Call-To-Action* (CTA) control frame to all MTs belonging to the current sector. The CTA frames serve as an invitation, signaling all the mobile terminals in the sector that they may prepare to communicate. By sending this frame, the AP effectively broadcasts its readiness to handle data from the MTs, encouraging those devices ready to transmit (Active MTs) to respond. The active MTs, reply to CTA by sending *Request-To-Send* (RTS) control frame back to the AP. The RTS frames are sent by each MT to inform the AP that they wish to start transmitting data. The exchange of CTA and RTS frames establishes a basic form of communication coordination. However, because more than one MT may respond with RTS frames at roughly the same time, the collision probability increases during this stage. Collision probability refers to the chance that two or more MTs will attempt to send their RTS frames simultaneously, causing their signals to interfere with each other.

After a certain time, the MTs will receive a *Clear-To-Send* (CTS) control frame from the AP containing the exact time to send its data so they do not interfere with each other. This time slot allocation is key to avoid data collision, which occurs when multiple MTs attempt to send data simultaneously. Collision problems are common issues in wireless networks, as shared channels can become overloaded when multiple devices try to communicate at once. By using CTS frames, the network limits these collisions to the control frames stage. This way, collisions are minimized during the actual data-sending stage, where larger amounts of data are transmitted. Once all data is received from the MTs, the AP sends an *Acknowledgement* (ACK) frame back to each MT. The ACK serves as confirmation that the data was successfully received and processed. After the current batch of MTs has been handled, the AP shifts its focus to the next sector. The sector-based protocol is particularly useful in directional antenna systems, where the AP can focus its signals in specific directions to optimize communication with MTs in different areas. By repeating the same process in each sector, the access point can sequentially manage the MTs in various zones without overloading the communication channel, enhancing network efficiency and reducing wait time for each MT.

The ADAPT MAC protocol enhances traditional IEEE MAC protocols by incorporating the CTA signal before RTS, which synchronizes the contention period for RTS transmission. This technique is akin to slotted ALOHA, but instead of longer data frames, ADAPT uses shorter RTS frames, reducing the likelihood of collisions. Conversely, IEEE MAC protocols without CTA frames lack this

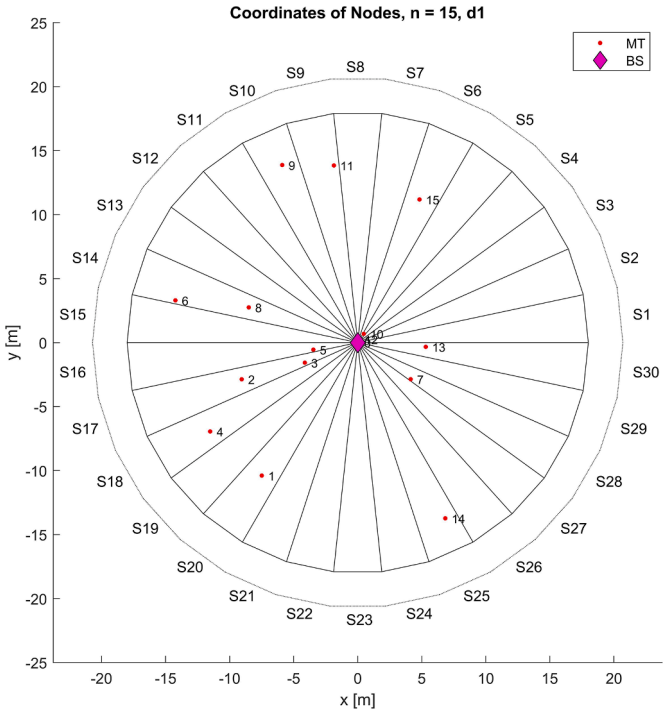

Fig. 3. The spatial distribution of MTs (centered topology, n = 15), AP is symbolized with a diamond in the center having a few cm the side length. There are 30 sectors around the AP, where the number of MTs per sector might be zero because of the low population density.

Table 1
Parameters used by the simulation.

Parameter	Name	Parameter Type	Parameter Values
L	Packet size	Fixed	65,000 Bytes
R_{Tx}	Transmission Rate	Fixed	69.12 Gbps
r	Cell Radius	Fixed	18 m
N	Number of Sectors	Fixed	30
φ	Angle of the Sector	Fixed	12°
t_{sec}	Sector Time	Fixed	3470 ns
t_{sim}	Simulation Time	Fixed	10 ms
n	Number of MTs	Variable	{15, 30, 60, 120, 240, 480, 960}
d	Topology Type	Variable	{d1, d2}

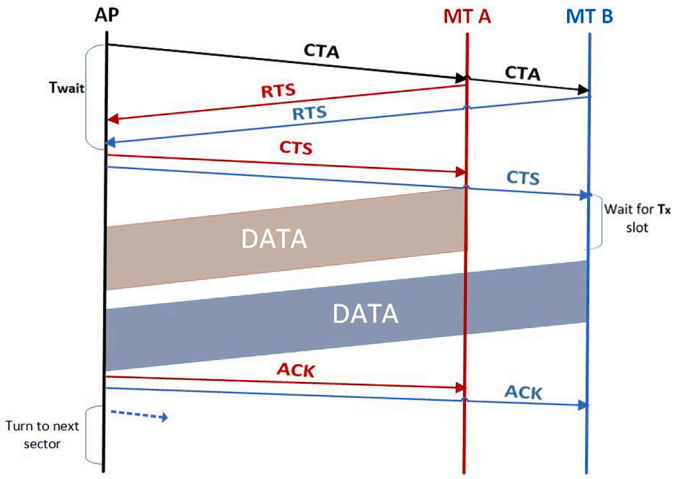

Fig. 4. The MAC mechanism of the ADAPT protocol. In each sector determined by an angle φ, specific signals are sent. CTA is launched by the AP at the beginning of the3-way handshake protocol to call MTs to request access to the channel.

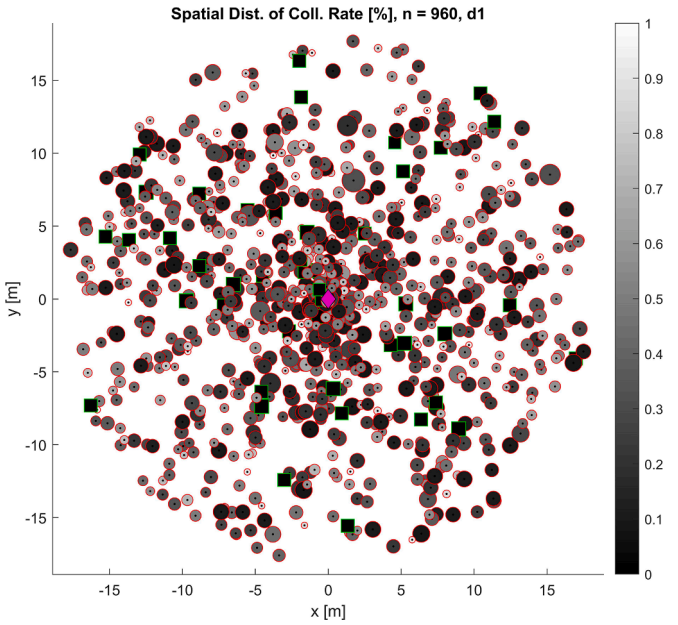

Fig. 5. Spatial distribution of collision rates of MTs in centered topology (n = 960). Darker bubbles indicate lower collision rates and size proportional to successful transmissions.

synchronization, leading to a higher probability of collisions during unsynchronized RTS transmission. ADAPT's approach enhances efficiency, especially in high-traffic conditions.

3.2. Key property data of the MAC mechanism

As previously mentioned, the collision rate increases at the control frame stage, Figs. 5 and 6 represents the collision rate spatial distribution having the highest MT number ($n = 960$), using the two different topologies: centered topology and uniform topology, respectively. The two figures contain the following information:

i) The diamond in the center symbolizes the AP.
ii) Black squares are the MT with no collisions.
iii) Bubbles represent the MTs that were experienced at least once during the control frame.
iv) Square and bubble size are proportional to the successfully transmitted data frames.
v) Grayscale shading of the bubbles indicates the collision rate value, a darker color signifies a lower collision rate.

In both figures, most small bubbles are lighter in color, indicating higher collision rates for these MTs and, correspondingly, a lower rate of successful transmission. This observation aligns with the expectation that MTs with higher collision rates tend to have reduced transmission success. Interestingly, the distribution of the collided MTs is random, having no connection with the topology type and it is considerable to be uniform in angular coordinates. This might happen because the closer MTs to the AP still belong to different sectors causing them to collide at a similar rate as MTs in more distant regions. Moreover, the number of non-collided MTs is evenly distributed radially regardless of the topology type, which arises from the uniform angular distribution of the MTs.

This analysis highlights a key takeaway: the proximity of the MTs to the AP alone does not directly reduce the collision rate, as nearby MTs in different sectors still experience similar collision probabilities. Moreover, the even radial distribution of non-collided MTs across both topologies confirms that a uniform angular spread of MTs can mitigate collision concentration in specific areas. These observations emphasize the need for strategies that address sector-based collisions specifically, rather than focusing solely on distance-based solutions. In all, the figures validate that the uniform distribution of MTs aids in balancing collision rates, making these insights valuable for optimizing future topologies and collision mitigation techniques.

Varying in the MTs number, it was necessary to calculate the population density parameter based on the area of the circle A ($\rho = n/A\ [m^{-2}]$). Increasing the population density outcomes in increasing the collision rate linearly independent of the topology type and that is what Fig. 7 shows, however, the uniform distribution topology has a higher collision rate of 20 % than the centered topology.

Moreover, ADAPT struggles with the compounded and progressively worsening effect of congestion in situations with large population densities, which is not usual with the traditional random MAC mechanisms used in practice (i.e. IEEE 802.11, IEEE 802.3… etc.).

Nevertheless, the transmission duration (the delay) of the successfully transmitted data frames in case of high population density

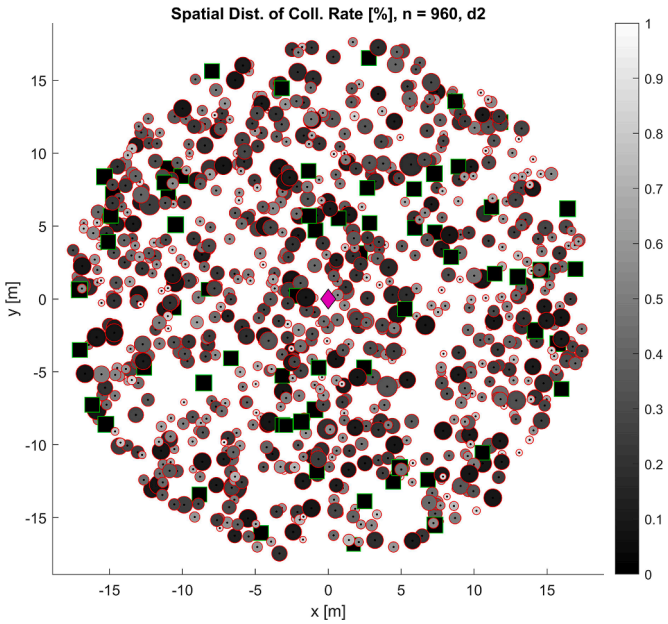

Fig. 6. Spatial distribution of collision rates of MTs in uniform topology (n = 960). Squares are the MTs without collisions. AP is placed in the center, represented by a diamond.

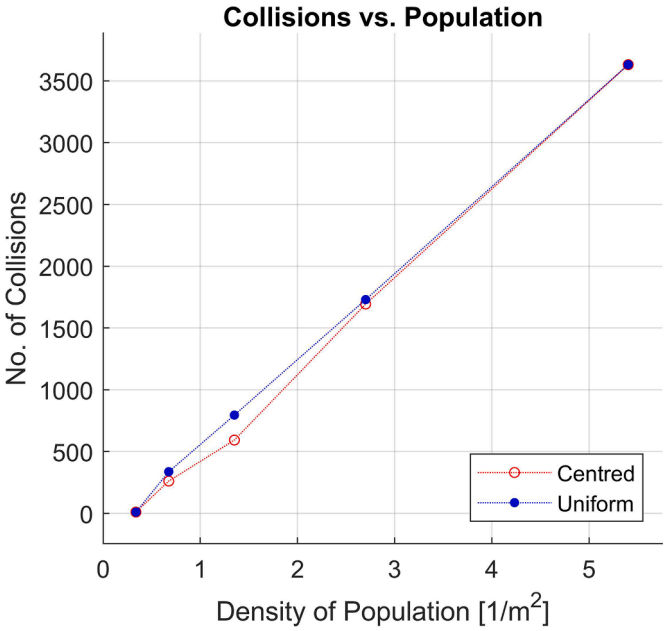

Fig. 7. Impact of population density on collision rate: higher density increases collisions; uniform topology shows 20 % more collision than centered topology.

also increases linearly as time increases having a slope $m_0 = 0.88$ (see Fig. 8).

Having a small number of MTs will cause no delay time in the transmission time (see Fig. 9) while increasing the MTs will cause an increase in the slope (m_0) having a logarithmic dependency. Meanwhile, the topology type made no significant difference. Furthermore, analyzing the received power by the MTs shows that it has fractal patterns (shown in Fig. 10) motivating us to study it in multiple resolutions as well as applying wavelet transform.

These findings are crucial for improving the MAC protocol in high-density networks. Understanding how the MT density impacts

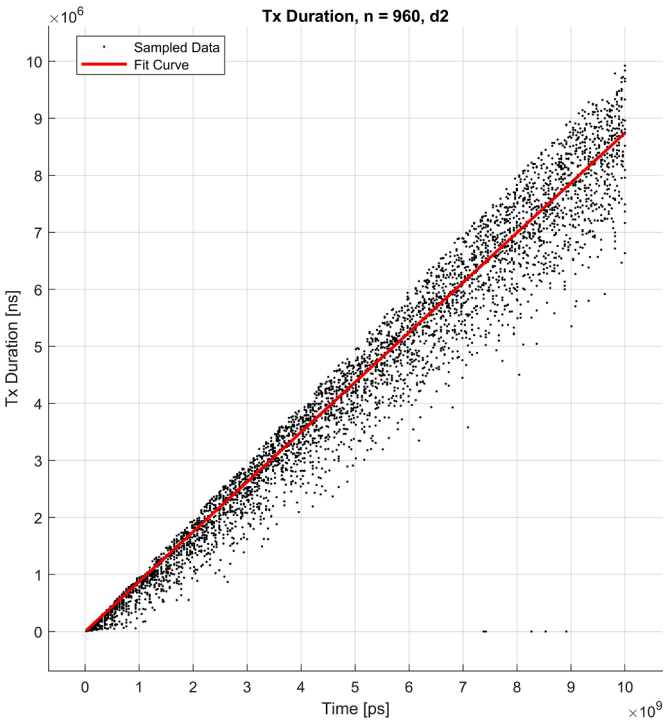

Fig. 8. Effect of high population density on transmission duration: linear increase in delay with population density, slope $m_0 = 0.88$.

Fig. 9. Impact of MTs number on the slope of transmission duration: logarithmic increase in delay with MTs, independent of topology type.

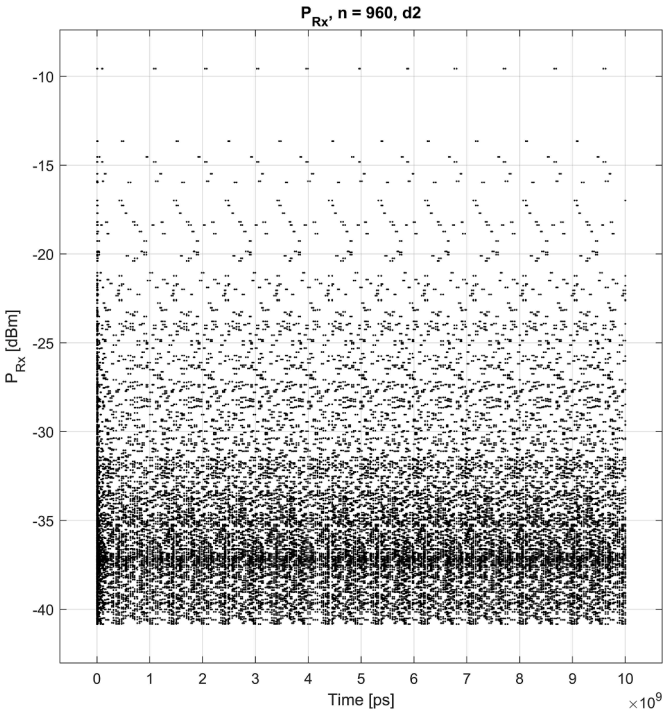

Fig. 10. Fractal patterns in received power by MTs.

collision rates, delay, and signal patterns can help design the protocol that minimizes congestion and improves efficiency. Insights into fractal patterns in received power suggest multi-resolution analysis that could enhance the protocol's adaptability and performance in dense environments, leading to more reliable and efficient wireless networks. Overall, this development will support diverse applications, enable scalability, and create a robust, efficient wireless communication ecosystem for the future.

3.3. Dual-parameter integration-based MAC analysis

To enlarge the visibility of ADAPT properties and enhance the study we suggested adding two different parameters to the macroscale code:

Overlapping ratio, *m*: Is introduced as a critical parameter to enhance the transmission opportunities for the MTs by allowing consecutive sectors to overlap. Every consecutive sector overlaps with a ratio m (see Figs. 11 and 12) for increasing the transmission opportunities of the MTs having the following equation:

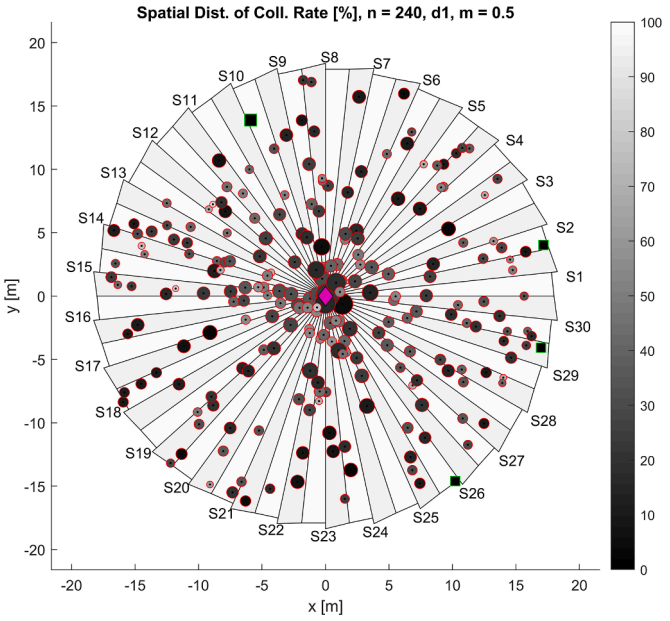

Fig. 11. Spatial distribution of the collision rate, centered topology (s, n, m) = (1, 240, 0.5). The overlapping ratio is indicated by grey sectors having spikes.

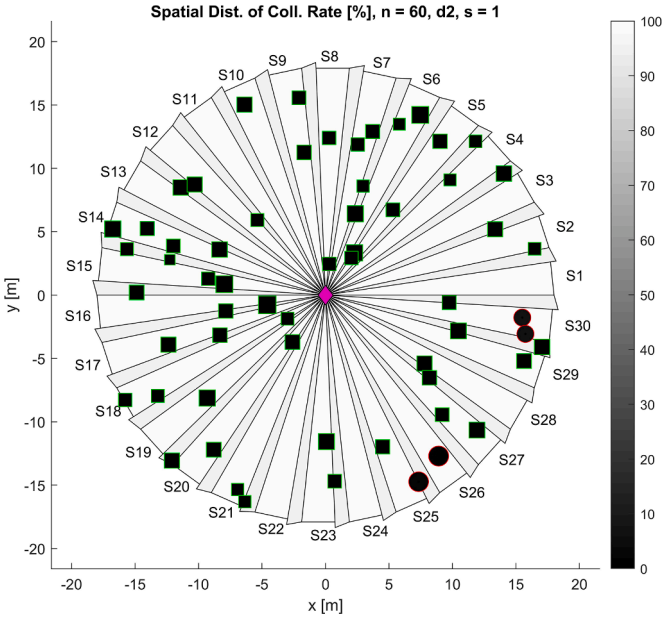

Fig. 12. Spatial distribution of the collision rate, uniform topology (s, n, m) = (1, 60, 0.3). The size of the bubbles and squares is proportional to the transmission rate.

$$m = \frac{A_{i+1}}{A_i} \tag{1}$$

A_i represents the area of the sector $i = 1, \ldots, N$, where m takes the values $m \in \{0.1, 0.3, 0.5, 0.7, 0.9\}$. The essence of adding the overlapping ratio lies in its ability to create a more flexible and robust communication environment. By doing so, the MTs at the edge of one sector can still maintain a connection with the AP while transitioning to the adjacent sector, hence reducing the likelihood of dropped connections during movement or when initiating transmission. This strategy increases the spatial reuse of the communication medium, effectively multiplying the transmission opportunities for MTs by supporting them with a border coverage area. Meanwhile, also it can help mitigate the impact of interference by spreading transmission across overlapping sectors which can be particularly

beneficial in high-density environments where congestion is a concern. However, In highly congested areas, it might degrade the overall throughput. Additionally, managing the complexity of more active transmission may complicate resource allocation and scheduling, offsetting the intended benefits of improved coverage.

Rotation step, s: represents the step that the AP takes in rotating between the sectors, defined with the following equation:

$$s = a(t_{i+1}) - a(t_i)(mod\ N) \tag{2}$$

Where $a(t_i)$ is the index of the sector at a certain time moments t_i, and it takes the values $B = \{1,7,11,13,17,19,23,29\}$, choosing these values gives important properties for the set, one can observe that the elements of the set i are all prime except $s = 1$. Set B has a twin relation meaning that when you sum opposite position elements gives back always number of sectors N = 30 (1+29 = …= 13+17 = 30). Based on the algebraic Galois field, having an initial element a_i between 0 and $N-1$ we always get back to the exact same element a_i after the N step, the reason behind this property is the periodic rotation of the AP between the sectors.

The incorporation of the step parameter lies in its ability to facilitate periodic sector access, ensuring that the AP effectively covers all sectors without bias. By choosing values that are primarily prime, the rotation pattern minimizes collisions, enhancing transmission opportunities while maintaining a balanced load across sectors. Furthermore, the periodic nature of the rotation guarantees that starting from any initial sector index $a(t_i)$ (within the range of 0 to $N-1$), the AP will cyclically return to the same sector after N step. This end ensures the consistency of the communication opportunities for the MTs as the AP systematically rotates, optimizing resource allocation and reducing latency by allowing time for MTs to prepare for transmission as the AP approaches their sector. All in all, we could say that this rotation step improves coverage efficiency and enhances sector management while contributing to a more dynamic and responsive network architecture. Despite that, this parameter adds complexity to the system, its periodic nature limits flexibility, making it difficult to adapt to dynamic network conditions which can be adapted based on real-time traffic demands.

We plotted the dependency of the collision rate of the sectors and the MTs in Figs. 13 and 14, respectively, as it has been said earlier, as the MTs increase the collision rate gets higher and higher, and when the cell contains a small number of MTs, no collision exists. However, the collision rate is dependent on the overlapping ratio parameter in cases when we have medium population density. Understanding these dependencies is important for optimizing network performance, as it enables the design of strategies that mitigate collisions, ensuring smoother communication and improved reliability in high-density environments.

Equivalently is happening in Figs. 15 and 16, which shows the dependence of the collision rate of the sectors and MTs on the rotation step s respectively, higher population leads to a higher collision rate, and low population density has a small collision rate, but still collision rate behaves randomly as we increase the rotation step in medium population density, however, we can say that it is kind of symmetric to step $s = N/2$, where the reason is caused by the twin relation that exists in the step set. Recognizing these patterns is essential for refining sector rotation strategies and enhancing collision management, ultimately leading to improved network efficiency and performance.

The plotted figures demonstrate how varying these parameters impacts network performance, with the overlapping ratio

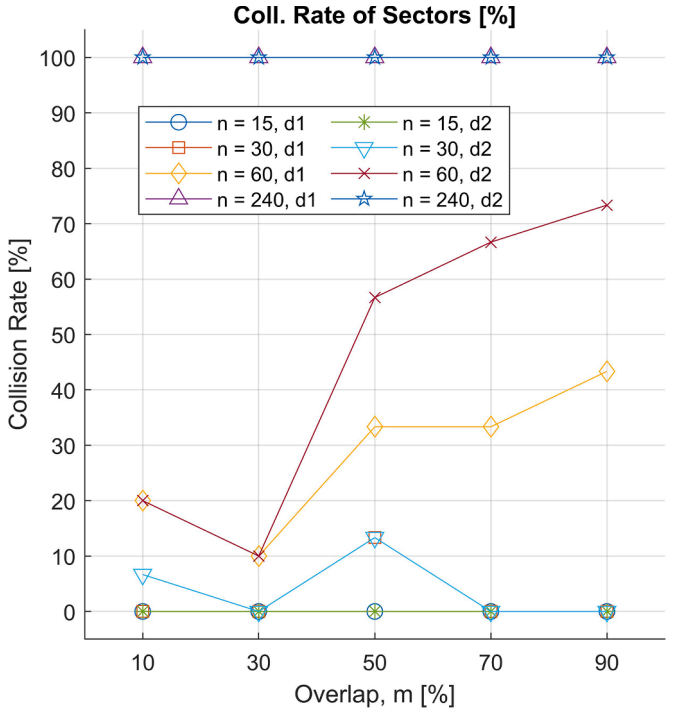

Fig. 13. The dependence of the collision rate of sectors on the overlapping between consecutive sectors (s = 1).

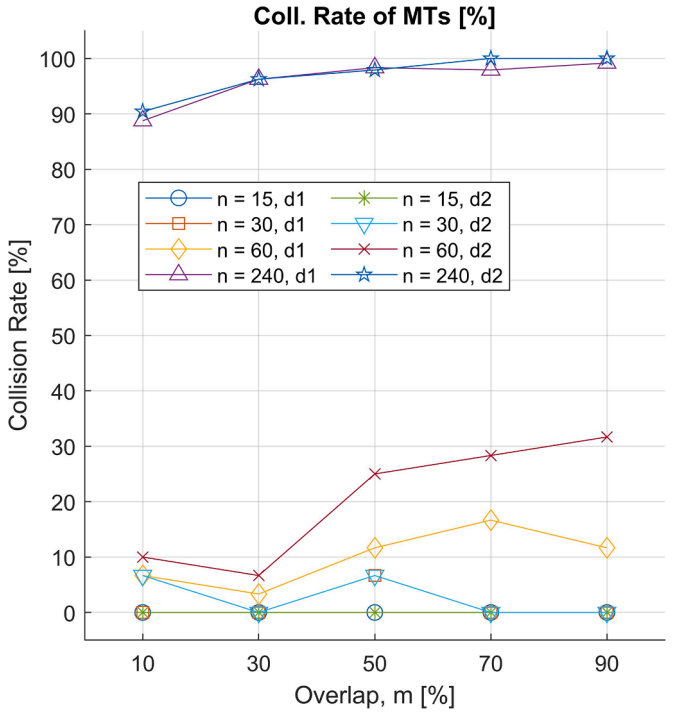

Fig. 14. The dependence of the collision rate of MTs on the overlapping between consecutive sectors (s = 1).

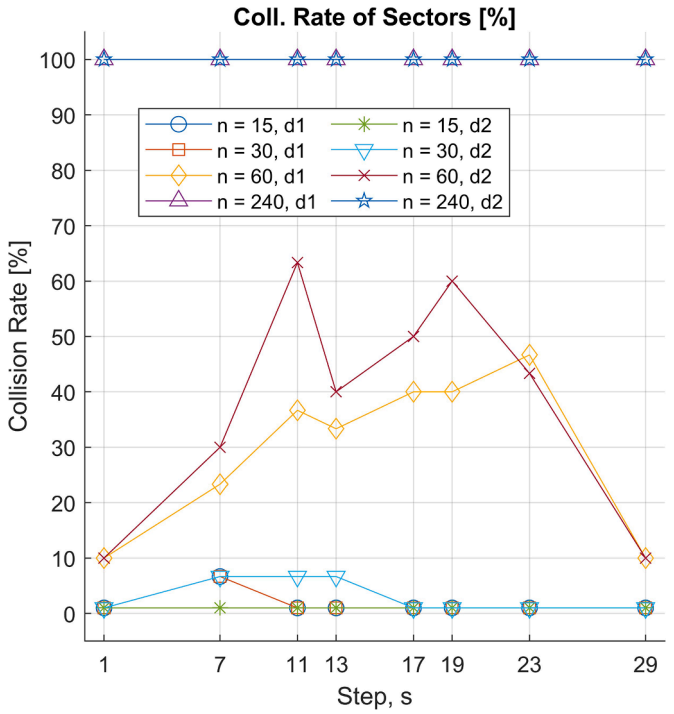

Fig. 15. The dependence of the collision rate of sectors on step size, s. increasing in collision rates is correlated with increasing in MTs in sector level.

enhancing the coverage and the rotation step ensuring systematic access to all sectors.

As observed, a higher MT population leads to an increased collision rate, while lower densities reduce collision significantly. Correspondingly, the interactions between these parameters reveal intricate dependencies that can be leveraged to refine network

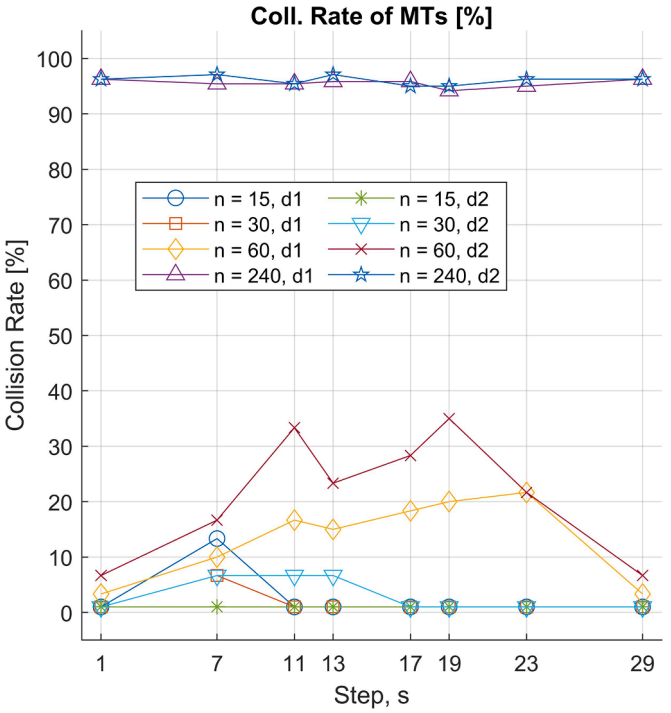

Fig. 16. The dependence of the collision rate of MTs on the step size, s. increasing in collision rates is correlated with increasing in MTs in the whole system.

strategies.

3.4. Inter-subsystem shannon entropy behaviour of the ADAPT system

Shannon entropy and information theory offer valuable methods for analyzing subsystem interactions in the wireless networks field. It quantifies uncertainty, helping assess data transmission efficiency, while information theory uses mutual information to examine how changes in one subsystem impact the other. These metrics enable real-world benefits, such as adaptive protocols that respond to network load variation, reduce interference, and improve reliability. In this subsection, we delve deeper into how Shannon entropy and mutual information can be applied to model and optimize the behavior of the overlapping ratio and the subsystems in communication systems, examining the effect on the received power, collisions, and network stability.

Calculating the Shannon entropy of the ADAPT mechanism helps in studying the efficiency of the MAC protocol where it can be optimized to reduce collisions and idle times. Adding the overlapping ratio parameter to the ADAPT protocol will divide the MTs into two different subsystems; Normal MTs (N) are the active mobile terminals that belong to only one sector having only one chance for communication per rotation, and Lucky MTs (L) are the active mobile terminals that locate on the overlapping area which make it belong to two different sectors, this property allows it to communicate with the AP two times per rotation. Should be mentioned that an active set of nodes is randomly elected at each rotation time. Two consecutive rotations have different active mobile terminals in the ADAPT cell around the AP. Analyzing the interdependence between these two subsystems using Shannon entropy could benefit in understanding how would they influence each other and aid in balancing the load of the overall system. Therefore, we concentrate on evaluating the received power of the MTs by the AP during the communication period in each sector $e = 1, 2, \ldots, 2900$. Shannon entropy of the two subsystems (S_N, S_L) are given by the following formulae:

$$p_i^N[e] = \frac{P_i[e]}{\sum_{j=1}^{k} P_j[e]}, \; i = 1, 2, \ldots, k \tag{3}$$

$$S_N[e] = -\sum_{i=1}^{k} p_i^N[e] \cdot \log\left(p_i^N[e]\right) \tag{4}$$

$$p_i^L[e] = \frac{P_i[e]}{\sum_{j=k+1}^{n} P_j[e]}, \; i = k+1, k+2 \ldots, n \tag{5}$$

$$S_L[e] = -\sum_{i=k+1}^{n} p_i^L[e] \cdot \log(p_i^L[e]) \tag{6}$$

We note that any entropy (equations: (4) and (6)) is a non-negative number and a zero entropy may be in a situation when no active MT exists ($p[e] = 0$) or just one active MT exists ($p[e] = 1$) in the zone of overlapping sectors. By active MT we mean a node wanting to send data to the AP and its RTS control frame sent back to the AP is non-colliding. In these two cases $p[e] \cdot \log(p[e]) = 0$. For the case $p[e] = 0$ the zero entropy value is an asymptotic limit. In the previous equations the total entropy of the whole subsystem is as follows:

$$p_i[e] = \frac{P_i[e]}{\sum_{j=1}^{n} P_j[e]}, \ i = 1, 2, \ldots, n \tag{7}$$

$$S_{Tot}[e] = -\sum_{i=1}^{n} p_i[e] \cdot \log(p_i[e]) \tag{8}$$

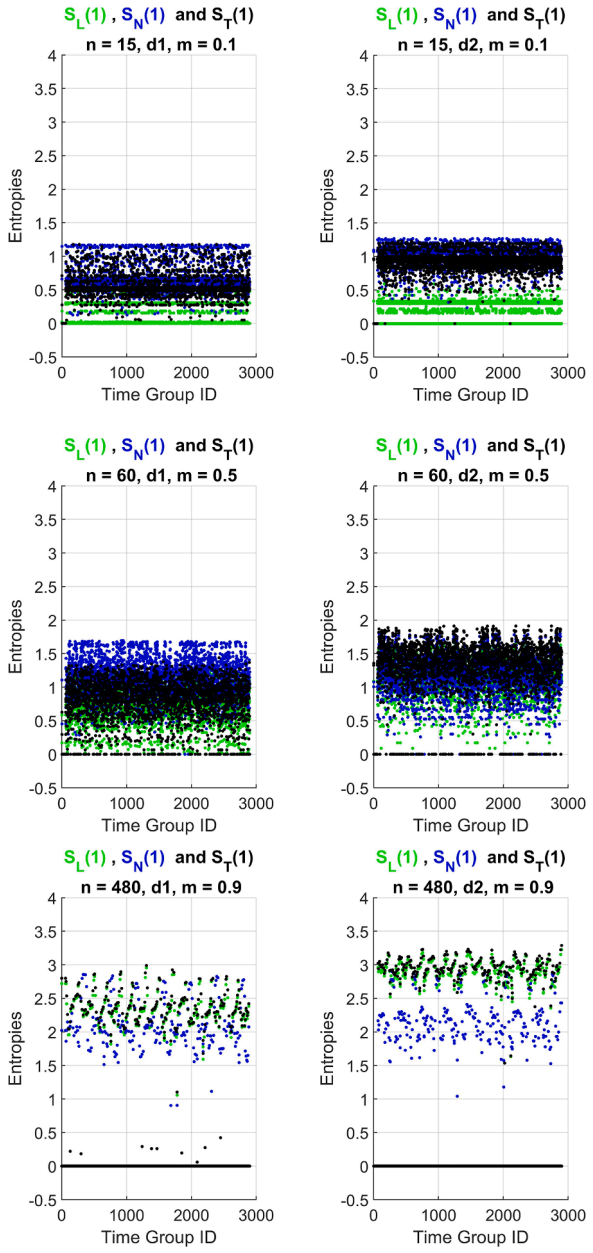

Fig. 17. Entropy analysis of subsystem interdependence for six simulation cases.

$P_i[e]$ is the received power of the MT i by the AP in each sector e, where $S_N[e]$, $S_L[e]$ and $S_{Tot}[e]$ represents the entropy of the normal MTs, lucky MTs, and the total mobile terminals, respectively, and p_i^N, p_i^L and p_i represents the probability variables of the normal MTs, lucky MTs, and overall system, respectively in each sector e, having the following property:

$$\sum_{i=1}^{k} p_i^N[e] = \sum_{i=k+1}^{n} p_i^L[e] = \sum_{i=1}^{N} p_i[e] = 1 \tag{9}$$

In the case of independence of the two subsystems, the validity of the following relation is considered:

$$S_{Tot}[e] = S_N[e] + S_L[e] \tag{10}$$

We quantitatively evaluate the interdependence of the separated subsystems by examining the entropy, as shown in the Fig. 17, where we thought of studying different internal aspects like randomness, stationary, or the existence of any patterns. Hence, using the Phillips-Perron test we calculated the stationarity of the entropies by a binary digit where 0 – non-stationary and 1- stationary which are written inside the parentheses of in the following figures: Figs. 17–20, also we have noticed the presence of patterns during the

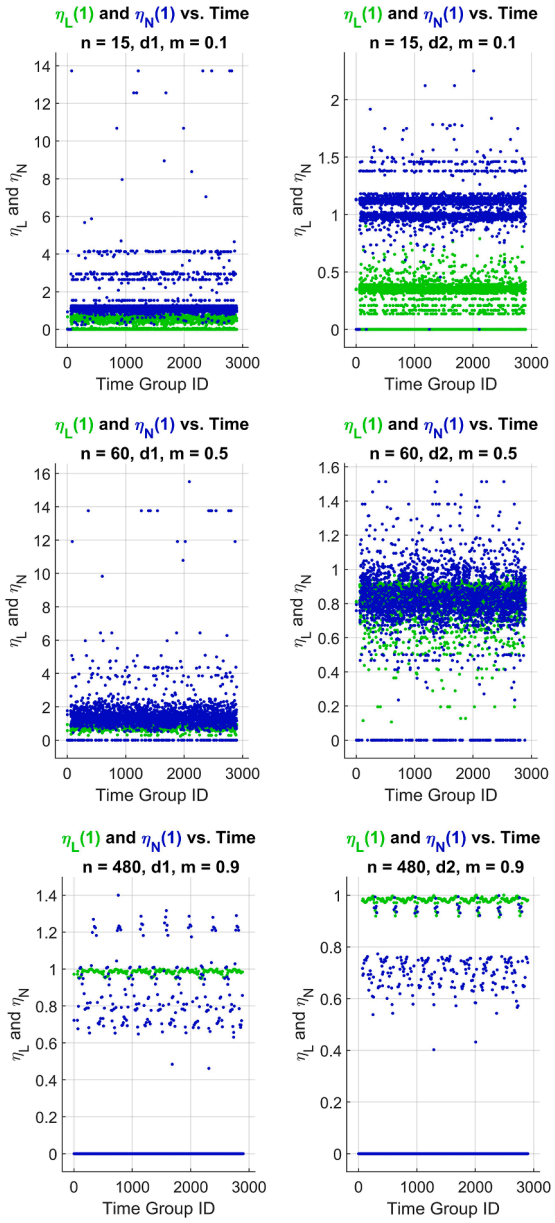

Fig. 18. Entropy ratios analysis of subsystem interdependence for six cases.

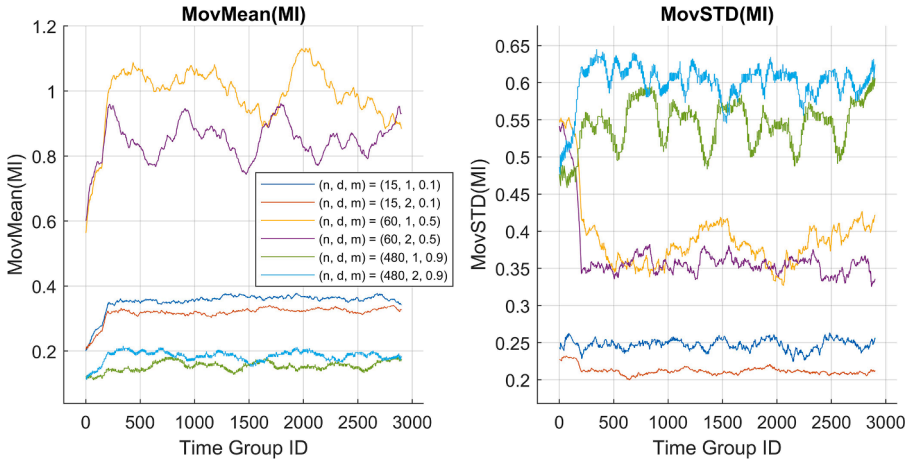

Fig. 19. Moving mean (a) and moving standard deviation (b) of mutual information of L and N subsystems (the legend in between in for both figures).

complete rotation of the MAC protocol due to the periodicity spin that the AP makes. Zero entropies in Figs. 17–18 present zero or just one active MT in the sector zone corresponding to the time group. The order of dots plotting to represent entropies in Fig. 17 is lucky MTs (green), normal MTs (blue), and then all MTs (black). If the total entropy is zero, then both lucky and normal entropies might be zero and black dots hide other dots. When only lucky MTs have zero entropy, then total entropy is greater than zero and green gots are visible (n = 15 and n = 60 in Fig. 17).

For larger population cases (n > 60 in Fig. 17) rare green dots are hidden by the black dots. The reason is that population increase may cause collisions more frequently and that leads to a higher number of zero total entropies. However, the entropy values increase with the population density. Also, the topology type has a global impact on the entropies: d2 has greater values with 12 % as for d1. In the case of d1 (centered) topology the density of MTs around the AP is greater than for d2, implying a higher probability of collisions in that region. The number of remaining active MTs becomes small, resulting lower number of positive terms in the formule (4), (6), and (8).

The entropy difference approaches zero as the two subsystems' independence increases:

$$\Delta S[e] = S_N[e] + S_L[e] - S_{Tot}[e] \tag{11}$$

The mutual information (*MI*) measures the amount of information between two subsystems, quantifying their dependence. It helps identify how much knowing one variable reduces uncertainty about the other. *MI* has relationship with Shanon entropy based on Eq. (11), as it was mentioned in [36]:

$$I[e] = S_N[e] + S_L[e] - S_{Tot}[e] \tag{12}$$

In this Eq. (12), $I[e]$ denotes the *MI* that captures the overlap information between the N and L subsystems, reflecting their interdependence. A higher $I[e]$ implies a stronger connection, while a lower $I[e]$ suggests greater independence between subsystems.

Fig. 19 (a) and (b) depict the moving mean and moving standard deviation, respectively, of the *MI* between the two subsytems across six different cases. In Fig. 19 (a), the moving mean of the *MI* decreases as the overlapping ratio increases. This trend indicates that greater overlap between the sectors reduces the interdepence, as more overlap creates redundancy, leading to less unique information shared between them. Converely, Fig. 19 (b) shows that the moving standard deviation behaves differently, it peaks at the highest overlapping ration of $m = 0.9$, indicationg greater variability in the *MI* due to the pronounced interactions and redundancy in highly overlapping scenarios. The overlapping ratio of $m = 0.1$ has intermediate variability, suggesting moderately dynamic interaction. Interestingly, the lowest variability occurs at an overlapping ratio of $m = 0.5$, implying that the middle-ground overlap stabilizes *MI*, balancing shared and unique information dynamics. Together, these two figures demonstrates how the extent of subsystem overlap influence both the average interdependence and its variability, reflecting the complex interplay between redundancy and distinctiveness in *MI*. The interplay of overlapping ratio *m* offers valuable insights into system performance, which highlights how varying in this parameter impact the stability and variablity of *MI*.

Based on the calculated entropy of the two subsystems in Eqs. (4) and (6), and the total entropy in Eq. (8) of the ADAPT system we compute the entropy ratio as follows:

$$\eta_N[e] = \frac{S_N[e]}{S_{Tot}[e]} \tag{13}$$

$$\eta_L[e] = \frac{S_L[e]}{S_{Tot}[e]} \tag{14}$$

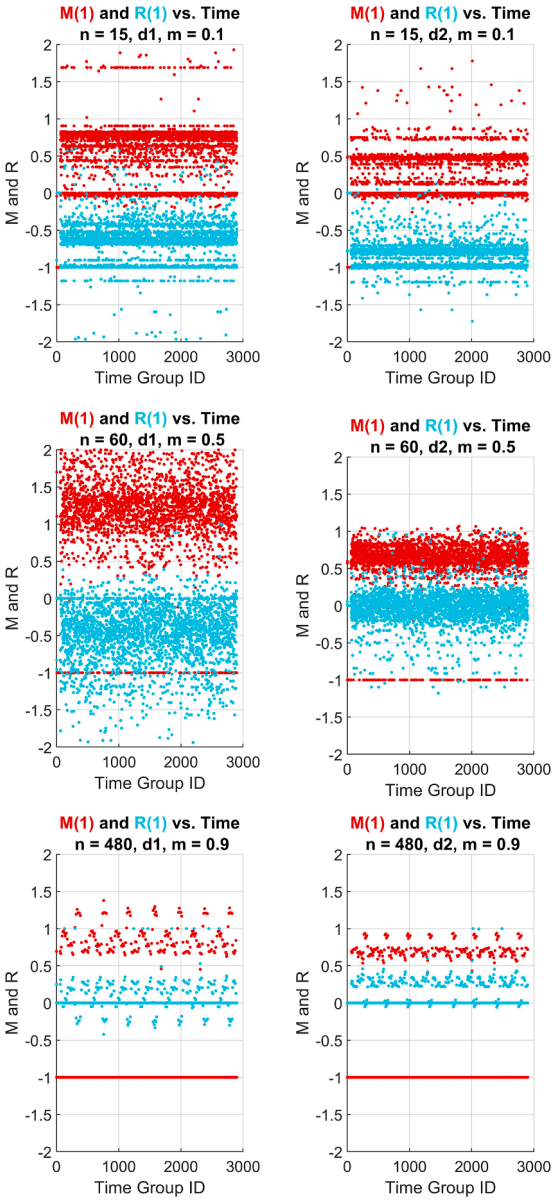

Fig. 20. Entropy ratios-based metrics behavior for six different simulation cases.

The entropy ratio is the entropy of the two calculated subsystems over the total entropy of the system. By dividing the combined entropy of the subsystems by the overall system's entropy, these ratios offer insight into the degree of interdependence or independence between the two subsystems. A high entropy ratio suggests that the subsystems are relatively independent, as their combined entropy approaches the total system entropy (see Fig. 18, entropy ratios for the active normal MTs (blue dots) for low to medium population density (15 and 60)). Conversely, a low entropy ratio indicates strong interdependence, meaning that information or changes in one subsystem significantly influence the other (see Fig. 18, entropy ratios for the active lucky MTs (green dots) for most of the cases), the higher entropy ratio for the active normal MTs compared to the lucky MTs likely stems from the limited access opportunities active normal MTs have. Since active normal MTs can only communicate with the AP at most once per rotation, their chances are constrained, leading to higher uncertainty in the access success. In contrast, The active lucky MTs have a more predictable access pattern, reducing their entropy ratio. This difference suggests that access reliability is higher for the active lucky MTs, while the active MTs face more variability. In rare cases (like in Fig. 18, the case having 480 MTs, overlapping ratio 0.9, and uniform topology) higher entropy ratio for active luchy MTs may occur due to increased congestion or interference in overlapping area, causing more variability in their access attempts.

We calculated a metric called the Inter-Subsystem Mutual Effect (M) to evaluate the mutual effect between the two subsystems using the following formula:

$$M[e] = \eta_N[e] + \eta_L[e] - 1 \tag{15}$$

The inter-subsystem mutual effect metric evaluates the interdependence level between the two subsystems, M being closer to zero indicates a high level of interdependency (see Fig. 20), conversely, more analysis needs to study the significance of nonzero M.

The inter-subsystems mutual effect quantifies the interaction strength between the two subsystems. M being 0 $(M = 0)$ indicates minimal or no mutual influence, suggesting that the two subsystems function independently without affecting each other's entropy significantly. For $M = -1$, we have both entropy ratios of the subsystems N and L equal to zero, meaning no active MT exists or just one active MT exists in the N and L subsystems. Another important information is that the metric M is strongly related to the low-pass filter (LPF), as it aggregates the influence of both subsystems and smooths out rapid fluctuations in entropy ratios, reflecting a long-term mutual effect. This end aligns with *LPF* characteristics, which capture low-frequency trends over time. As the number of MTs increases, the M metric stabilizes between 0.5 and 1 for centered topology (shown in Fig. 20) . This observation indicates that with more MTs, the mutual influence between these subsystems becomes more pronounced, leading to consistent interaction patterns that enhance communication efficiency across different topologies. Also, this concentration reflects a system nearing equilibrium, where interactions among normal and lucky MTs become more predictable.

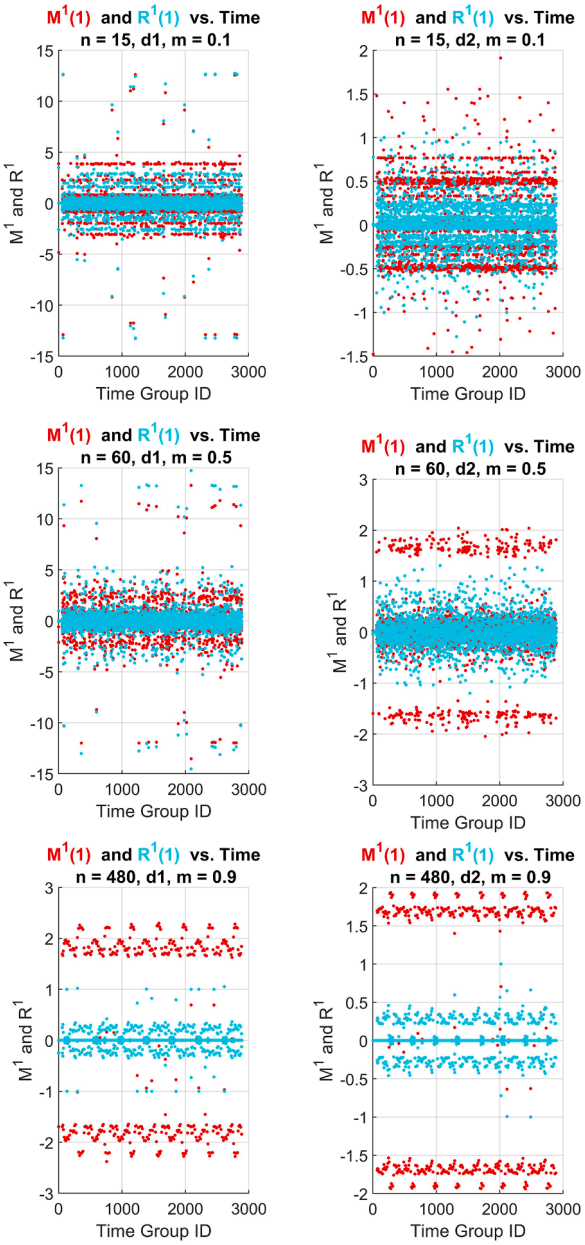

Fig. 21. The first derivative of entropy ratios-based metrics behavior for six different simulation cases.

Moreover, the Relative Entropy Difference (R) calculates the balance of the system (see Fig. 20), we calculated it based on the following formula:

$$R[e] = \eta_N[e] - \eta_L[e] \tag{16}$$

R being closer to 0 declares the equilibrium of the two subsystems, this suggests that both subsystems experience similar uncertainty and variability in accessing the AP, reflecting a balanced communication opportunity. Such equilibrium minimizes congestion and interference, promoting stable network performance and ensuring fair resource distribution among MTs. In contrast to the M metric, the R metric calculated as the difference between the entropy ratios of normal and lucky MTs, functions similarly to a high-pass filter (*HPF*). Case $(R = 0)$ means the entropies of the N and L subsystems are the same, $(S_N = S_L)$. Highlighting the variability and sharping the contrasts between the susbsystems entropy levels, detecting high-frequency shifts that indicate immediate difference in access opportunities or congestion impact. In low population density scenarios, the R metric shows more negative values than positive ones, suggesting that the active normal MTs have more predictable access patterns compared to lucky MTs. Nevertheless, as population density rises, R approaches 0, indicating a more balanced communication opportunity for both subsystems. This shift occurs due to increased competition for resources, which leads to a more equitable distribution of access opportunities as the network becomes denser.

It is so important to study the behavior of both introduced entropy ratio metrics, therefore, we tend to write both metrics in matrix form, and this is what the matrix equation presents:

$$\overline{D[e]} = \overline{T} \cdot \overline{\mathrm{H}[e]} + \overline{C} \tag{17}$$

Having $\overline{D} = \begin{pmatrix} R \\ M \end{pmatrix}$ and $\overline{\mathrm{H}} = \begin{pmatrix} \eta_N \\ \eta_L \end{pmatrix}$, both of them being time-dependent, while $\overline{T} = \begin{pmatrix} 1 & -1 \\ 1 & 1 \end{pmatrix}$ and $\overline{C} = \begin{pmatrix} 0 \\ -1 \end{pmatrix}$ being constant, the transformation (16) is about making rotation by $\pi/4$ firstly, then zoom in with $\sqrt{2}$ secondly and shifting toward $-\infty$ in the dimension of M by one unit lastly. This transform magnifies and presents the entropy ratios's behavior in the new state space given by the {*M, R*} metric pair. By highlighting shifts and patterns, the {*M, R*} pair helps to discover dependencies and dynamic interactions between subsystems, that can be leveraged to optimize communication protocols, reduce interference, and enhance overall network stability. The usefulness is supported by the observed patterns in the plotted figures of M and R (Fig. 20) that dmonstarte system stability and equilibrium under varying conditions. These results confirm that the matrix transformation effectively highlights the balanced interaction between subsystems, making it an essential tool for optimizing system performance and stability.

Furthermore, Studying the derivatives of the metric pair would emphasize more in its behavior (see Fig. 21), therefore we have the following formulae:

$$M^1 = \Delta M = \Delta\eta_N + \Delta\eta_L \tag{18}$$

$$R^1 = \Delta R = \Delta\eta_N - \Delta\eta_L \tag{19}$$

One can notice, that by calculating the derivative, the scale got enlarged guarding the original pattern depending on the simulation scenario case and the parameters *m, n*, and *d*. This scale adjustment brings subtle variations into clearer focus, revealing periodic shifts and fluctuations that may otherwise be overlooked. This finding is crucial for tracking rapid changes in entropy ratios, enabling fine-tuning of parameters for enhanced adaptability and robustness in practical applications.

The suggested Shannon entropy metrics are closely tied to the overlapping ratio in the 6G MAC mechanism, reflecting how various subsystems interact and share resources. These metrics offer quantitative means to evaluate the communication power and performance of the mobile terminals within the ADAPT system. The derivative of entropy ratios quantifies the divergence or difference in information flow between subsystems, making it crucial to understand how well the MTs can maintain robust communication under different transmission conditions. The relation between the entropy metrics {*M, R*} and {*LPF, HPF*} helps in analyzing the communication dynamics. The *LPF* emphasizes the steady-state behavior and tends to information flow, allowing for a clearer understanding of how subsystems stabilize over time. Meanwhile, *LPF* shows rapid changes and anomalies, providing insight into transient behaviors during peak loads. Ultimately, these insights not only enhance our understanding of subsystem dynamics but also inform the development of adaptive strategies that can optimize resource allocation and improve overall network reliability and efficiency in future wireless communication systems.

3.5. Limitations and extension possibilities

TeraSim is a *ns*-3 extension for simulating in THz-band communication networks, while TeraSim is a powerful tool, it has several limitations. Simulating large-scale networks can become computationally intensive due to the large number of devices, and the need for detailed modeling can lead to slower simulations, raise the complexity of the tool, and increase resource consumption. Moreover, TeraSim does not directly interface with real-world THz communication hardware, which limits its use in experimental validations and real-world testing. Meanwhile, it does not provide highly sophisticated models for mobility in dynamic environments, especially in case of the nanoscale scenarios where movement can significantly impact performance. It lacks support for simulating security protocols or attacks, this aspect is important for communication networks, particularly in sensitive applications like healthcare or military nanonetworks. Despite its limitations, TeraSim is the first dedicated environment for THz communications, offering essential tools to explore more the unique challenges of THz frequencies, such as the high bandwidth and absorption losses. The different integrated

models made it invaluable in advancing THz research, setting a foundation for future, more refined simulations in this emerging field.

Equivalently, a notable limitation of the ADAPT protocol is its focus only on the uplink communications, lacking the downlink strategy integration. This approach restrict its application, as balanced two-way communication is a must for most of the real-world network scenarios. Futur extensions of the work could address ADAPT's current limitations by integrating the downlink communication mechanism. Extending the simulation time beyond the current 10 *ms* would enable more comprehensive analysis, which could yield improved understanding and refinements in resource allocation, collision management, subsystems mutual effectiveness, and enhancing the robustness of the ADAPT protocol in a dynamic network environment.

One aspect could be interesting to study higher derivatives order and see its impact and behavior. Future work may also focus on the analysis of other different mutual information methods like transfer entropy (*TE*), pointwise *MI* (*PMI*), directed informtion (*DI*) and others. The aim is to explore their effectiveness in assessing interdependence in communication subsystems and compare it to the actual proposed entropy ratios's results. Moreover, a potential solution is the decomposition of the time series data into stationary intrinsic mode functions (IMFs), which involves breaking down the complex into simpler signals, making it easier to analyze and predict the behavior of the communication system under different conditions and gain deeper insights into how entropy-based ratio metrics can be optimized for real-world applications in the next 6G wireless communication networks. Machine learning can be also a modern tool to model the relation between these metrics and network performance, which leads to more adaptive and intelligent communication strategies. Conducting sensitivity analysis to identify which parameters most significantly influence the system's behavior may also prove the benefit of the metrics. Integrating these findings into network simulation tools can facilitate the development of enhanced protocols that dynamically adjust based on real-time network conditions, ultimately improving the efficiency and reliability of future wireless communications.

4. Functional roles of diverse AI methods in the 6G network analysis

Integrating AI in modern wireless technologies is highly recommended for enhancing network performance, where supervised and unsupervised ML can optimize various aspects. Hence, we applied different AI methods to different scenario cases for better analyses. By leveraging machine learning and data-driven approaches, we aim to gain deeper insights into network behavior, assess the effectiveness of entropy-based metrics, and identify potential strategies to enhance communication efficiency and reduce collision rate. It is important to mention that an increase in the number of MTs leads to a corresponding rise in computational overhead, therefore we vary the number of MTs in the following subsections based on the method employed to reduce computational demands. This variation allows us to assess the effects of MT scalability on overall system performance while optimizing resource utilization. This phenomenon is primarily attributed to the dependency of CPU instructions on the number of MTs. As the network scales and more MTs are introduced, we consider the number of MTs as a scaling parameter, which evaluates its impact on system performance. The processing requirements for managing communication, and data transmission intensify, thereby escalating the overall processing demands on the system.

4.1. Feature extraction with wavelet-based supervised learning

Wavelet transform has some important properties like the invariance to translation meaning that shifting events in time does not affect the result, and also stability to deformation which ensures that even when the data series is warped, characteristic patterns can still be effectively identified. Moreover, the wavelet transform offers localization in both time and scale, unlike the traditional focus on time and frequency. The wavelet transform relies on the convolution operation, that allows for converting a signal into a more refined form where features become more prominent, therefore using such a method for feature extraction helps in simplifying the task for the supervised neural networks, leading to more efficient and accurate classification. This method enhances the clarity of the signal, making it easier for the network to recognize and process key patterns.

The wavelet transform WT of the signal $x(t)$ is a mathematical tool well-known in the signal processing field, signal compression, and time-frequency analysis. Unlike the Fourier transform that analyses signals using sinusoidal functions, the wavelet transform uses a mother wavelet denoted as $\Psi(t)$, being an $L^2(\mathbb{R})$ function, as far as:

$$\int_{-\infty}^{\infty} |\Psi(t)|^2 dt < \infty \tag{20}$$

Wavelets $\psi_{a,b}(t)$ are specific subsets of the mother wavelet represented in Eq. (21):

$$\psi_{a,b}(t) = \frac{1}{\sqrt{a}} \Psi\left(\frac{t-b}{a}\right) \tag{21}$$

where pairs (a, b) are points in the half plane $\mathbb{R}_+ \times \mathbb{R}$. Parameter a and b are the scale and time shift, respectively. $\psi(t)$ in Eq. (21) satisfy the condition of mean zero and square norm one as represented in the following formulae:

$$\int_{-\infty}^{\infty} \psi(t) dt = 0 \tag{22}$$

$$\int_{-\infty}^{\infty} |\psi(t)|^2 dt = 1 \tag{23}$$

The signal $x(t)$ has projection onto the subspace of scale a conform to the next formula:

$$x_a(t) = \int_{\mathbb{R}} WT_\Psi\{x\}(a,b) \cdot \psi_{a,b}(t) db \tag{24}$$

Where t he wavelet transform of the signal $x(t)$ is the following:

$$WT_\Psi\{x\}(a,b) = \int_{\mathbb{R}} x(t)\psi_{a,b}(t) dt \tag{25}$$

The wavelet coefficients are $c_{jk} = WT_\Psi\{x\}(a,b)$, where $a = 2^{-j},\ b = k2^{-j}$ are the binary dilation and binary position, respectively. Reshape of the c_{jk} into a single vector is considered a feature vector, which is a compression of the (a,b) points set.

There are a lot of existing transformation methods that can be used for extracting features, well-known ones are the Fourier transform and short-time Fourier transform (STFT), so why we are using wavelet transform? One has to note that Fourier transform provides a global frequency representation but lacks temporal resolution, while STFT offers time-localized frequency information but struggles with the trade between time and frequency resolution. Conversely, wavelet transform effectively captures both transient and persistent features across varying time scales, making it superior for analyzing non-stationary signals and providing a nuanced representation of complex data.

4.1.1. Feature extraction methodology of the data set

The WT-based feature extraction has proved its efficiency in many fields. In the medical field, researchers in [37,38] achieved higher accuracy (< 98 %) using RNN models. These results highlighted the wavelet transform's capability to extract relevant features for accurate classification. This has inspired us to apply a similar method within the ADAPT critical in the THz communication. As mentioned earlier, the fractal property motivated us to study the pattern of the transmission distance of the AP-MT pairs. For the scenario, we have 14 different simulation cases where we considered two parameters: the population number $n = 15, 30, 60, 120, 240, 480, 960$, and two topology types, the centered topology *d1* and the uniform distribution topology *d2*. From the simulated cases, we randomly select 300 compacted sequences from the overall data, creating so called feauture vectors, represented as follows:

$$\delta^i = \left(\delta^i_1,\ \delta^i_2,\ \ldots, \delta^i_{300}\right),\ i = 1,\ 2,\ \ldots,\ 14 \tag{26}$$

Every sequence vector $\delta^i_j \in \mathbb{R}^{2000},\ j = 1, \ldots, 300$ has 2000 serial elements, where the vectors have been classified and mapped based on Table 2 having in total 5 different classes $(C_1, \ldots, C_5)$, the classes are carefully chosen based on the mobile terminals' densities.

For each vector δ^i_j, the applied wavelet transform creates a so-called feature vector $f^i_j \in \mathbb{R}^{238}$ having 238 instead of 2000 containing a more compressed manner of the feature characteristics. We taught the LSTM by selecting 50 % randomly the distance feature vectors, Using the third quarter for validation during the teaching while the remaining part we use it for testing the taught results. Table 3 shows the used parameters for the LSTM neural network.

Since the features are already extracted using the wavelet transform, The architecture of the RNN network remains straightforward, as shown in the Fig. 22. The streamlined design facilitates efficient processing without the need for complex modifications or extra layers.

The next subsection will present the results of the training and delve into the discussion and interpretation of the results. The accuracy and performance of the training will be highlighted and discussed with the effectiveness of the applied methodologies in meeting the objectives of the study.

4.1.2. Results and discussion

Hence, the learning and classification results of the RNN types: LSTM, BiLSTM, and GRU neural network are shown in the next figures, notably the plot emphasizes the exponential speed at which convergence occurs and the corresponding exponential decline in loss showcasing the efficiency of the learning method.

The training of the LSTM RNN model shows rapid increase in accuracy, demonstrating how effectively the extracted featured were identified (Fig. 23). This quick improvement suggests that the model quickly learned to recognize patterns in the data, making the

Table 2
Class mapping of the distance sequence.

Distribution (d)	Number of MTs (n)						
	15	30	60	120	240	480	960
1	C_1	C_1	C_1	C_2	C_3	C_4	C_5
2	C_1	C_1	C_1	C_2	C_3	C_4	C_5
Collision	0	0	~ 0	> 0	> 0	> 0	$>> 0$

Table 3
RNN neural network applied parameters.

Property	Value	Property	Value
SquaredGradientDecayFactor	0.99	Solver	ADAM
GradientDecayFactor	0.90	Mini Batch Size	2100
InitialLearnRate	0.02	MaxEpochs	100
No. Hidden units at L2	100	No. Classes at L3	100
GradientThreshold	1	No. Classes at L4	5

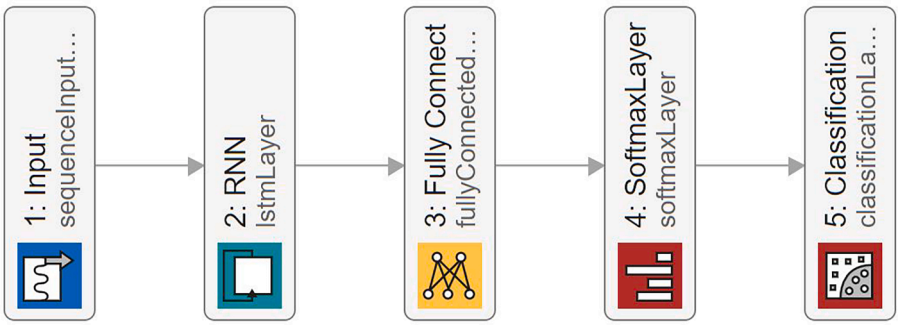

Fig. 22. Recurrent neural network structure example for LSTM, while the rest of the RNN types have the same structure, except layer 2.

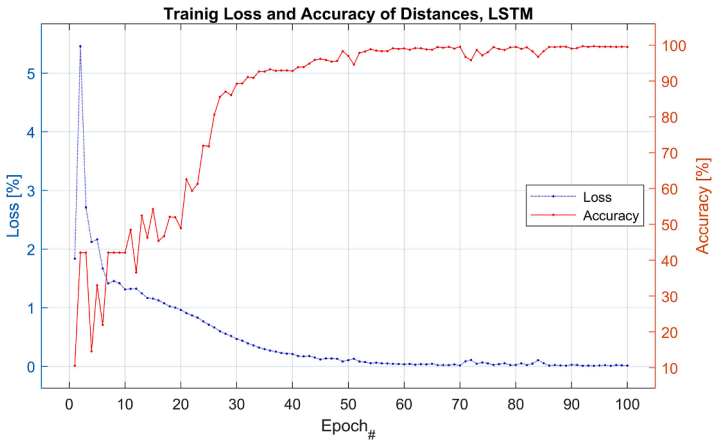

Fig. 23. LSTM neural network learning and classification results, highlighting rapid convergence and loss reduction.

training process efficient. The confusion matrix furthur illustrates the classification accuracy with 99.4 % testing accuracy, where most of the classifications were correct, with minimal confusion observed. A slight confusion was noted between some classes (Fig. 24).

Moving to BiLSTM model, the accuracy was good, but it faced some difficulties in learning the extracted features at the beginning, particularly until epoch 60. During this initial phase, the model struggled to effectively capture the nuances of the data. However, after epoch 60, the performnce significantly improved, and the learning accuracy surged to 99 % (Fig. 25). This indicated that, despiye early challenges, the model eventually adapted well to the features. The confusion matrix for the BiLSTM (Fig. 26) also reflected strong perfomance, showing an overall testing accuracy of 94.4 %. However, similar to the LSTM model, there was some confusion between certain classes, suugesting that while the BiLSTM achieved high accuracy, there remained small overlaps between specific categories that could be further refined.

The learning accuracy for GRU model followed a similar pattern to the BiLSTM, initially struggling but improving over time. Strating from epoch 70, accuracy increased to 99 % (Fig. 27). The confusin matrix showed the best testing accuracy of 99.5% with only slight confusion between class C_4 and C_5 (Fig. 28).

Each model, when combined with wavelet transform for feature extraction, showed strong performance. The GRU model, for instance, achieved 99.5 % accuracy and completed training and testing in a remarkably short time, highlighting its efficiency and ability to process complex data quickly. Similarly, the LSTM and BiLSTM models showed excellent accuracy, though with slight differences in training behavior. While all models demonstrated robustness in handling the given dataset, the wavelet transform required substantial computational resources. Additionally, class imbalance can affect model accuracy, especially for

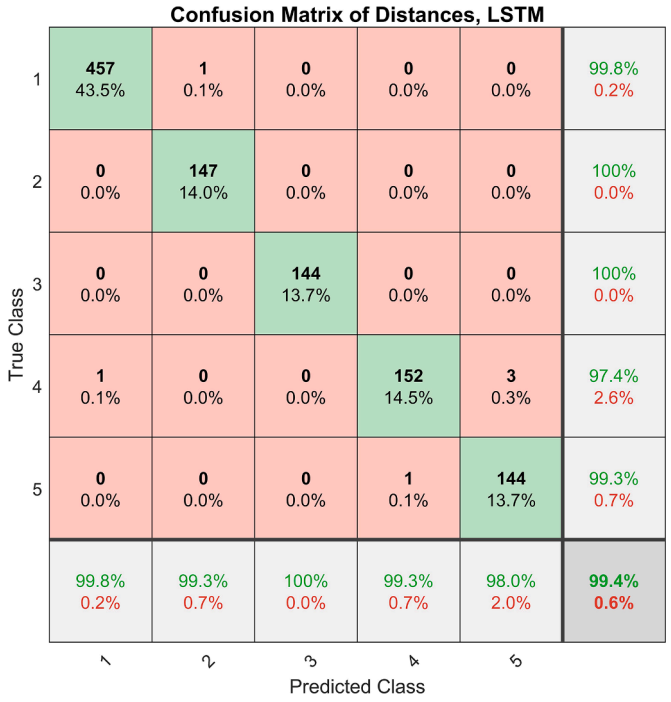

Fig. 24. LSTM confusion matrix illustrates classification accuracy, indicating high precision with minimal confusion.

Fig. 25. BiLSTM neural network learning and classification results, highlighting lower convergence and moderated loss reduction.

underrepresented classes. Although the GRU, LSTM and BiLSTM models performed strongly, their complexity may not always be justified in scenarios where the data does not have sequential dependencies. In such cases, simpler models could offer comparable performance with lower computational cost.

4.2. Feature analysis of ADAPT with unsupervised learning

Incorporating unsupervised machine learning into the ADAPT mechanism may enhance network efficiency in dynamic environments [39,40]. By leveraging data-driven insights, unsupervised ML-based clustering can help identify underlying patterns in network traffic and MT behavior without labeling the data. These aspects motivate us to apply the unsupervised ML on such complex data series to uncover hidden structures and correlations within the ADAPT protocol's communication patterns. Our main aim is to enhance protocol adaptability to fluctuating network conditions, optimize resource usage, and improve overall network performance. By doing so, we can enable the MAC system to self-tune its parameters in real-time, supporting more advanced techniques to the challenges inherent in Terahertz communications.

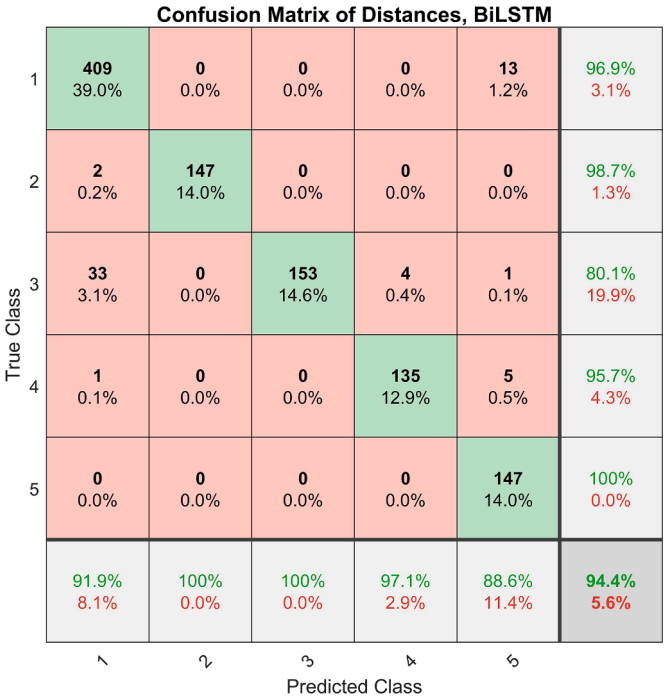

Fig. 26. BiLSTM confusion matrix illustrates classification accuracy, indicating lower precision with noticeable confusion.

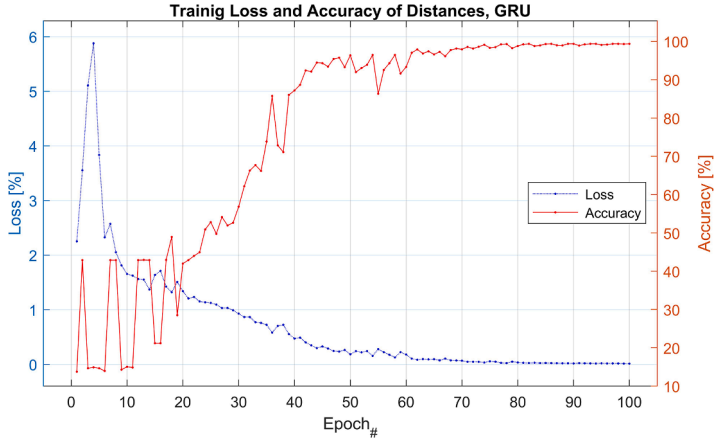

Fig. 27. GRU neural network learning and classification results, highlighting best convergence and loss reduction.

4.2.1. Feature analysis

Studying the sector behavior contributes to optimizing the ADAPT MAC mechanism and the THz radio channel. Within 50 simulation cases, having n ∈ {60, 120, 240, 480, 960}, d ∈{d1, d2} and $m \in \{0.1,\ 0.3,\ 0.5,\ 0.7,\ 0.9\}$, we calculated the sector efficiency considering both collisions and throughput as shown in Fig. 29 and Fig. 30 for gaining more insight into the efficacy and effectiveness of sector vectors.

Among the machine learning types, we have unsupervised machine learning where a given algorithm is trained on an unlabeled data set, which can discover hidden patterns and intrinsic structure of the trained data. Thus, in this section, we decided to use Density-Based Spatial clustering of applications with noise (DBScan) on the sector efficiency vectors for feature-based clusterization, DBScan clusters the data set based on the density of data points without the interference of the noise. Mainly, DBScan is sensitive to two parameters; the radius that defines the distance between two points to be neighbors, and the minimum points required to form a dense region or a cluster.

Analyzing the sector efficiency vectors using DBScan shows the high influence of the mentioned DBScan parameters on the number of clusters and the number of outliers shown in Figs. 31 and 32, respectively. The results show the effectiveness of the unsupervised DBScan machine learning, underscoring how crucial parameter selection is for successful data clustering. As shown in Fig. 33, the

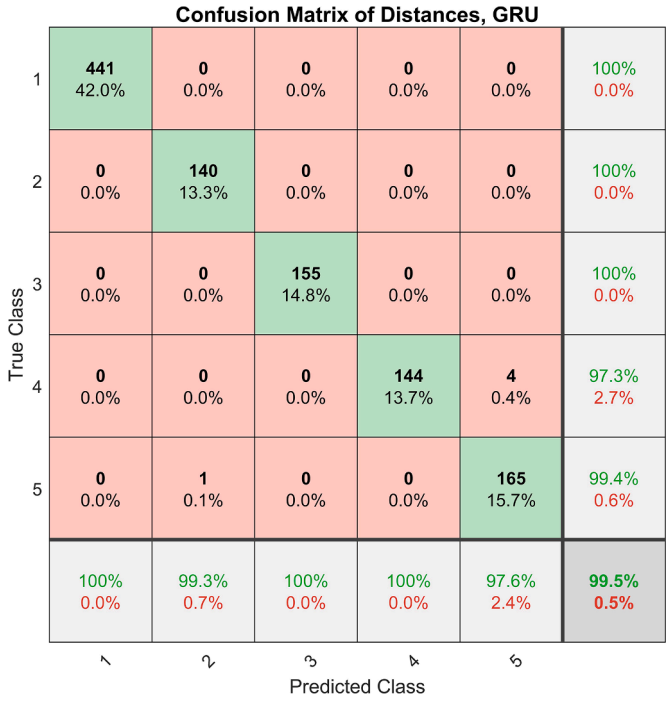

Fig. 28. GRU confusion matrix illustrates classification accuracy, indicating best precision with minimal confusion.

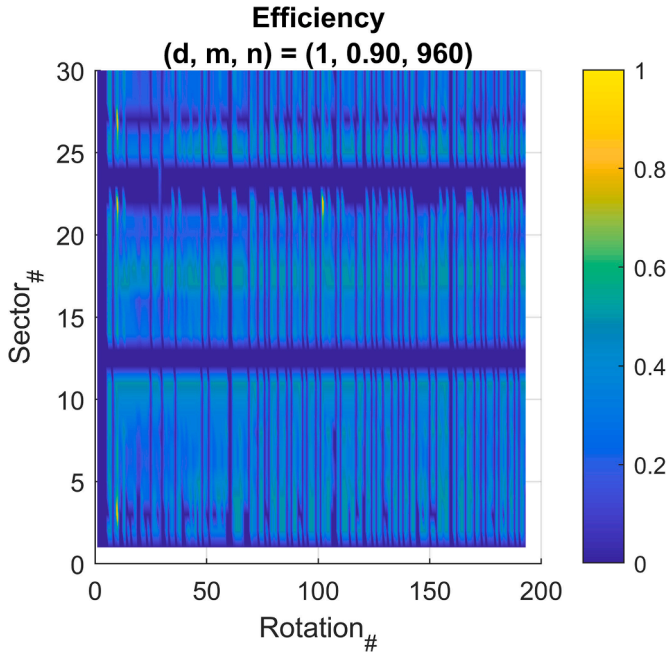

Fig. 29. Sector efficiency vs. rotation ID taking into consideration collision and throughput, for centered topology, overlap ratio m = 0.9, and highest population density.

number of clusters strongly depends on the cluster radius which requires a deep study and careful selection for accurate results.

Similarly shown in Fig. 34, where even the outliers got influenced, it is obvious when selecting the minimum number of points equal to 1, the number of outliers will be 0, the reason after that is that every element becomes a cluster itself and this is not logical therefore this option must be excluded.

Moreover, the relation between increasing the cluster radius and its impact on the number of outliers is evident, where a clear

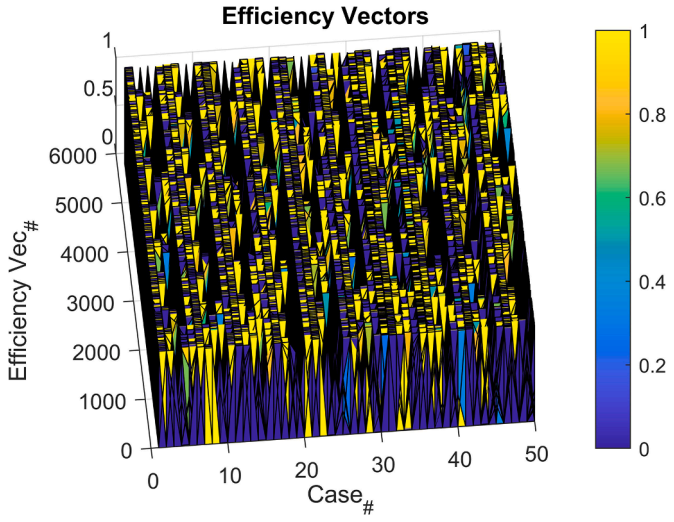

Fig. 30. Efficiency vectors for all 50 simulation cases. Elements in each dimension are numbers in the interval [0, 1].

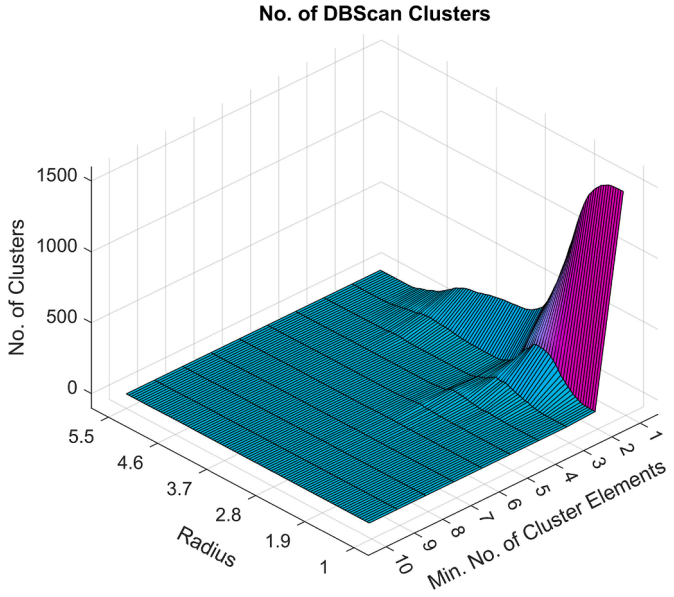

Fig. 31. DBScan clusters number vs. radius and minimum number of cluster elements, indicating the high dependency between the chosen DBScan parameters and the number of clusters.

reduction in both the number of clusters and the presence of outliers as the radius increases.

This finding highlights the importance of balancing the cluster radius with the minimum number of elements required for best classification. For achieving accurate data clustering, adjusting these parameters is a necessity.

4.2.2. Results and discussion

Hence, we explored how the number of outliers varies with changes in the minimum number of elements per cluster as presented in Fig. 35. The aim is to find the working point having the minimum number of outliers, As we exclude the number of elements being equal to 1 for the reason mentioned earlier, the working point is achieved by selecting 6 elements per cluster for sector efficiency vectors. Based on this, we define 7 different classes $(C_0, C_1, C_2, C_3, C_4, C_5, C_6)$of the data set, with outliers assigned to the class C_0. By doing so, the clustering process is enhanced offering valuable insights into the patterns of sector efficiency within the analyzed dataset.

The results of classifying the sector efficiency vectors using the working point are illustrated in Fig. 36, Given the substantial number of outliers which represents 25.5 % of the data (383 out of 1500 elements) revealed with dark blue rectangles in class C_0. Meanwhile, It is intriguing that sector efficiency vectors having the IDs 5, 15, and 25 are enrolled within the clusters C_4, C_5, and C_6. This criterion invites further investigation to understand why these sectors are enrolled in these classes in this manner, which could

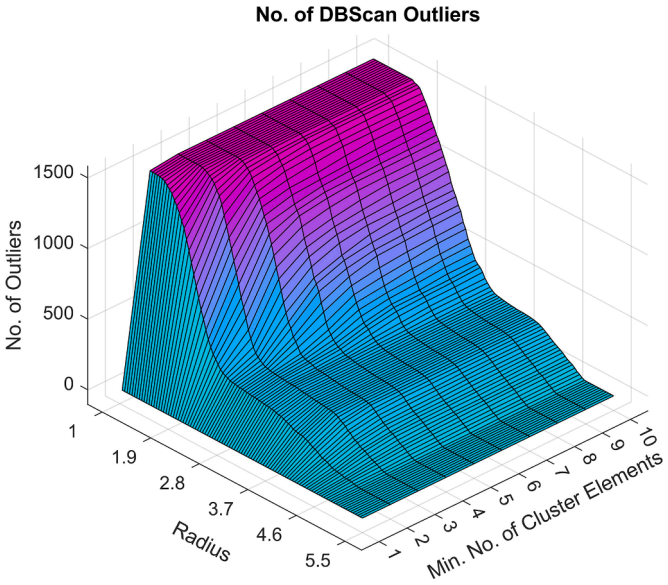

Fig. 32. DBScan outliers number vs. radius and minimum number of cluster elements, indicating the high dependency between the chosen DBScan parameters and the number of outliers.

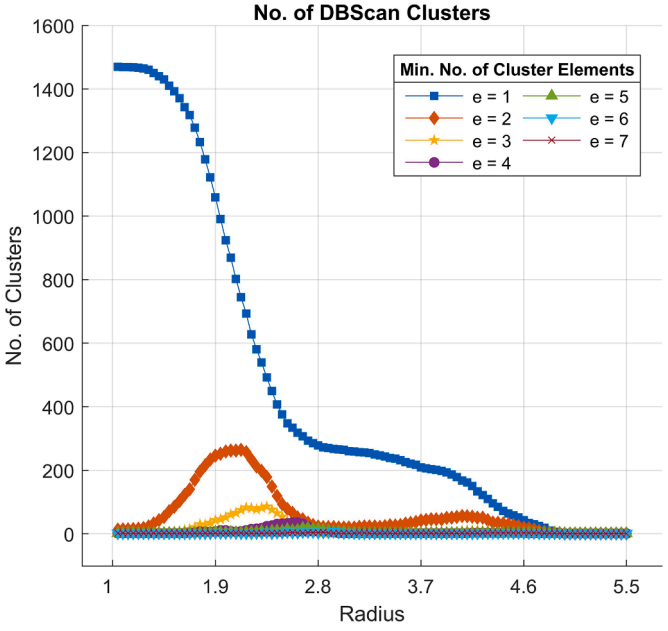

Fig. 33. DBScan clusters number vs. radius, shows how the number of clusters varies with changes in both the cluster radius and minimum number of cluster elements.

reveal unique characteristics or patterns specific to these cases and sectors.

We could say that DBScan suffers with data sets of varying densities and high dimensionality, making it sensitive to parameter selection and less effective for complex or large datasets. Future enhancement could include employing adaptive clustering algorithms that dynamically adjust based on real-time data variability or incorporating anomaly detection methods like: isolating forest, local outlier factor density-based method, and more, for handling and interpreting the outliers' meaning, thereby improving the precision and reliability of the clustering process.

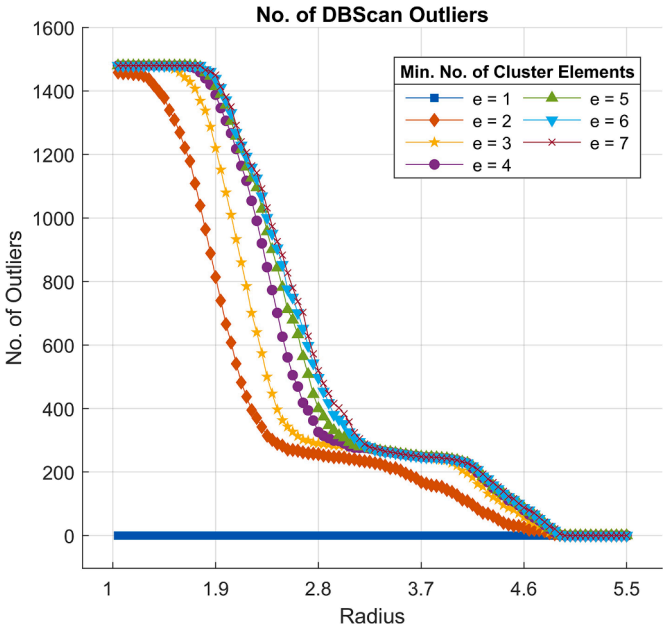

Fig. 34. DBScan outliers number vs. radius, shows how the number of outliers varies with changes in both the cluster radius and minimum number of cluster elements.

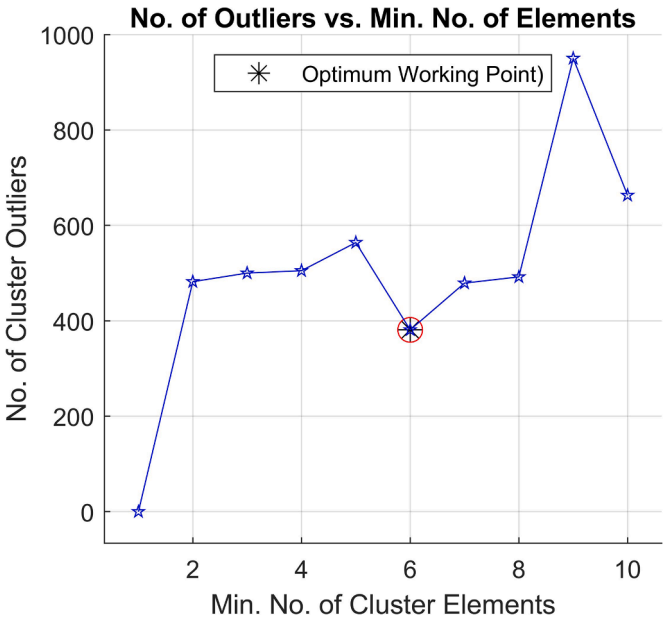

Fig. 35. Dependence of outliers number on minimum number of cluster elements, the optimum working point having a minimum number of outliers greater than 0 symbolized with a start inside the red circle.

4.3. Feature analysis with multi-layer transfer learning

Multi-layer transfer learning leverages pre-trained models to enhance the performance of complex systems by transferring knowledge from one domain to another [41–43]. We chose to implement ML-TL-based RNN in the ADAPT system to improve the efficiency and accuracy of the medium access control mechanism in wireless communication networks. We preferred to use RNN over CNN because RNNs are often less complex and require fewer parameters, since it focuses on the temporal dependencies of the data series rather than learning spatial hierarchies and patterns across multiple dimensions. Therefore, for applications like the ADAPT system, understanding the order and timing of data points is more important, and RNN provides a more suitable framework. Utilizing

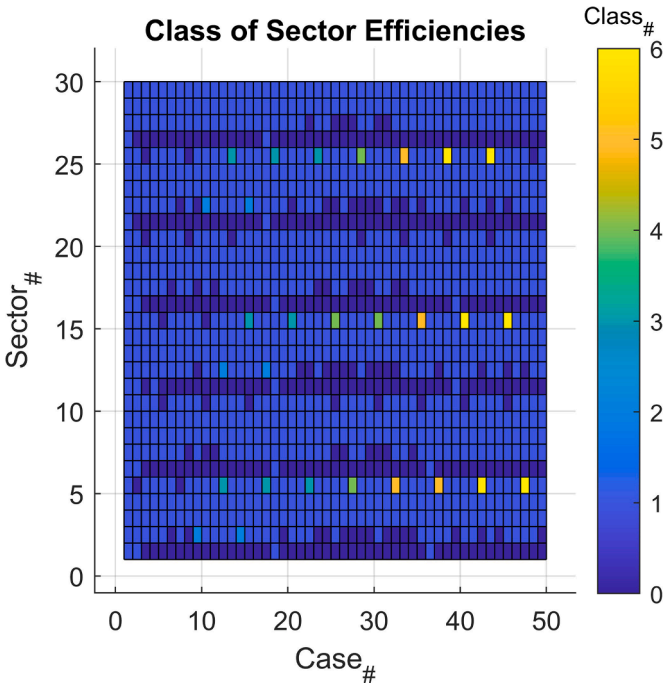

Fig. 36. Classification of sector efficiency vectors at optimal working point, having 7 different classes, with 25.5 % outliers in class C_0 marked by dark blue rectangles.

LSTM, BiLSTM, and GRU helps in capturing temporal dependencies and patterns within the data series. In the next sections, deeper insights and implementing methodology are explained, as well as the results and discussion.

4.3.1. *Feature analysis*

By adding the rotation step $s = \{1,7,11,13,17,19,23,29\}$, we took the most congested case having 960 MTs in 2 different topology types d1 and d2 having all together 16 cases. We considered to have four different classes of sector collisions in correlation with Table 4. For evaluating the transfer learning efficiency of the ADAPT MAC mechanism collision data series, we used three RNN types (LSTM, BiLSTM, and GRU). Each of these RNN types consists of one or more layers positioned directly after the input layer, enabling the network to capture sequential patterns in the data effectively. We added SoftMAx to finalize the output of the network, followed by Classification layers, which translate the learned representations from the RNN layers into actionable class prediction. The applied configuration allows for robust handling of complex time series.

By taking advantage of the taught layers, we envisioned a novel approach to constructing both homogeneous and heterogeneous multilayer neural networks through the transfer learning process. This innovation strategy not only broadens the scope of our neural network architecture but also enhances its adaptability to diverse datasets.

To evaluate the effectiveness and the goodness of the learning approach, we developed a comprehensive metric that quantifies the quality of the learning outcomes. The different types of TNNs employed in this endeavor are detailed in the Table 5. In addition, 'U' and 'T' are Untaught and Taught RNN types, respectively, the value after 'U' denotes the number of the untaught layers, and the value after the character 'T' states the number of RNN layers. The last column represents maximum epochs which increase with the increasing of RNN layers.

4.3.2. *Results and discussion*

After the training phase, we visualized the test accuracy by plotting the performance of both untaught single-layer and double-layer configurations of the different RNN types, coded in the Table 5 as 'U1' and 'U2', respectively. Notable, one untaught layer of BiLSTM outperformed the other RNN types achieving an impressive accuracy of 90.03 %, In contrast, the LSTM model recorded the lowest

Table 4
Classes sector collisions.

Class ID	Step Size, s	Sectors	Distribution	MT Number
1	1, 29	n = 30	d1, d2	N = 960
2	7, 23	n = 30	d1, d2	N = 960
3	11, 19	n = 30	d1, d2	N = 960
4	13, 17	n = 30	d1, d2	N = 960

Table 5
Neural network types.

NN Code	Transf. Learn.	Homogeneous	Taught Layers	Untaught Layers	Max. Epochs
U1	No	Yes	0	1	150
U2	No	No	0	2	150
T0	Yes	Yes	k = 1, …, 5	0	150+200·k
T1	Yes	No	k = 1, …, 4	1	150+200·k
T4	No	Yes	0	k = 1, …, 5	150+200·k

performance with a learning accuracy of 85.04 % (see Fig. 37). Moreover, adding another untaught layer to the neural network gave different results (see Fig. 38). Here, L1 and L2 refer to the first and second untaught layers of the RNN architecture. It is noteworthy that when LSTM is designated as L1, the testing accuracy is significantly influenced by the type of L2. In contrast, the type of L2 after BiLSTM (as L1) exhibits minimal impact on the results, while after GRU (as L1), the type of the untaught RNN layer (L2) influences both accuracy and testing outcomes.

For quantifying the goodness of the used RNN layers, and evaluating the internal performance of the chosen layers, we propose a metric to weigh the overall effectiveness of the method used. To the best of our knowledge, no similar metric exists in scientific literature to compare the performances. We decide to have a certain threshold constant $a = 0.90$ for validation purposes, which serves to calibrate our calculations and provide a consistent benchmark for evaluating the performance of the RNN layers utilized in our study, we calculate the Accuracy-to-Tima Ratio (ATR):

$$ATR_{valid}(a) = \frac{Acc_{valid}(a)}{Learn\ Time(a)} \quad \left[s^{-1}\right] \tag{27}$$

$$ATR_{test} = \frac{Acc_{test}}{Learn\ Time} \quad \left[s^{-1}\right] \tag{28}$$

We have $Acc_{valid}(a) = a$ and $Learn\ Time(a)$ represents the validation accuracy within a threshold a and learning time for the validation accuracy a, respectively. While Acc_{test} representing the testing accuracy after $Learn\ Time$ duration. The proposed metric so-called Weighted Accuracy-to-Time Ratio (WATR) is the weighted sum of the two calculated ATRs with a weight α:

$$WATR = \alpha \cdot ATR_{valid} + (1-\alpha) \cdot \ ATR_{test} \ \left[s^{-1}\right] \tag{29}$$

The weight α is objective that reflects the relative importance of validation versus testing performance. Given the significant impact of these parameters, we define α as the ratio of the validation and testing ATR values, calculated using the following expression:

$$\alpha = \frac{\max(ATR_{test})}{\max(ATR_{valid})} \tag{30}$$

By doing so, the high value of WATR indicates the high performance of the neural network with good testing accuracy and fast learning time. This is precisely the outcome we aim to quantify, as it reflects the effectiveness, goodness, and responsiveness of our model in practical applications.

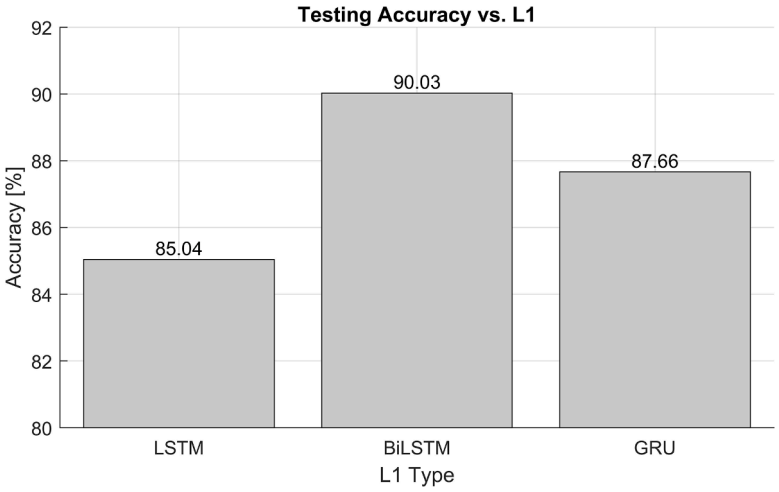

Fig. 37. Test accuracy of sector collisions for different U1 RNN types, BiLSTM achieved the highest accuracy of 90.03%. The decreasing orders are BiLSTM, GRU, and LSTM.

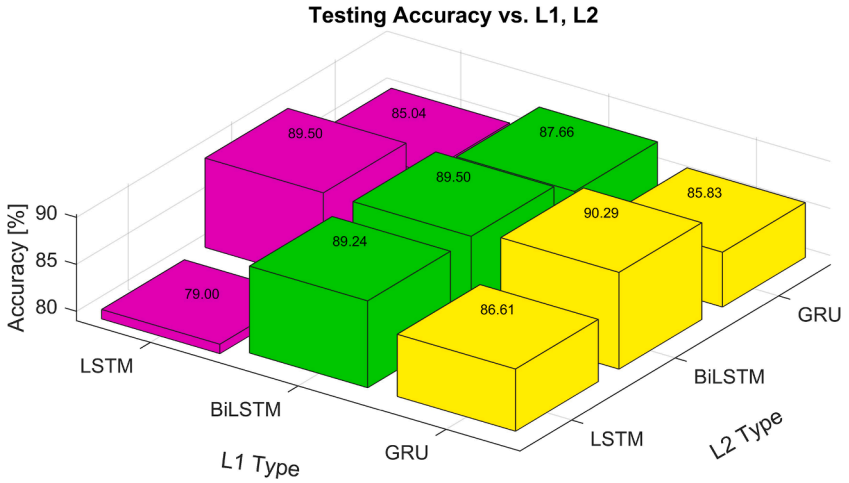

Fig. 38. Test accuracy of sector collisions for different U2 RNN type pairs, L2 has a significant impact when GRU is used as L1, but minimal effect when BiLSTM is used as L1.

To evaluate the performance and effectiveness of the taught and untaught layers being homogeneous and heterogeneous, the following figures plot the performance of T0, T1, and T4. One can notice, that in the case of the homogenous T0, increasing in the RNN layer despite the NN type, the learning time increases (see Fig. 39).

However, the testing accuracy decreases with the increasing of the taught layers, especially LSTM and BiLSTM, however, GRU performed better having 4 layers. A comparable pattern is noticeable for the learning time in the case of heterogenous T1 as we saw in T0 (see Fig. 40) with a 30 % reduced duration. Increasing the taught layers shows negligible accuracy impact in the case of BiLSTM and GRU, while the accuracy of LSTM becomes less as we increase the layers.

We evaluate the performance of both T0 and T4 by calculating the WATR metric, and the results are shown in the Fig. 41. For both cases, GRU performed better than the other NN types with a slight difference between having one and two layers, however, since the learning time increases with more layers', higher testing accuracy is indicated for $k = 2$.

Moreover, the goodness metric for U2 NN demonstrates the best performance when GRU layers are used, the optimal configuration is achieved when both layers are GRU having WATR $= 0.11\ s^{-1}$ (shown in Fig. 42). For heterogeneous T1 NN, as the number of taught layers increases the WATR value, the goodness metric value decreases. In all, this study revealed that increasing the number of RNN layers can lead to longer learning time. The type of the RNN significantly influences testing accuracy and WATR performance metrics. Notably, GRU outperformed other configurations, demonstrating superior efficiency and accuracy in both homogeneous and heterogeneous setups.

The findings are particularly beneficial for the ADAPT mechanism and for future 6G applications, as they highlight optimal neural network configurations for effectively managing complex data series. Further analysis is planned to assess the impact of the weight α on the optimal WATR metric value, this investigation will help refine our understanding of how the weight α influences the overall

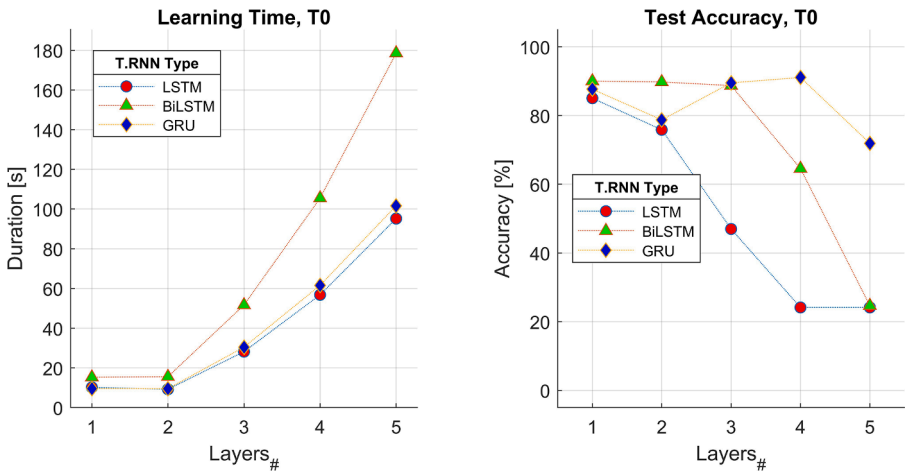

Fig. 39. Learning time (Left) and test accuracy (Right) of sector collisions for different T0 RNN types; increasing the number of RNN layers, regardless of the NN type, leads to a rise in learning time.

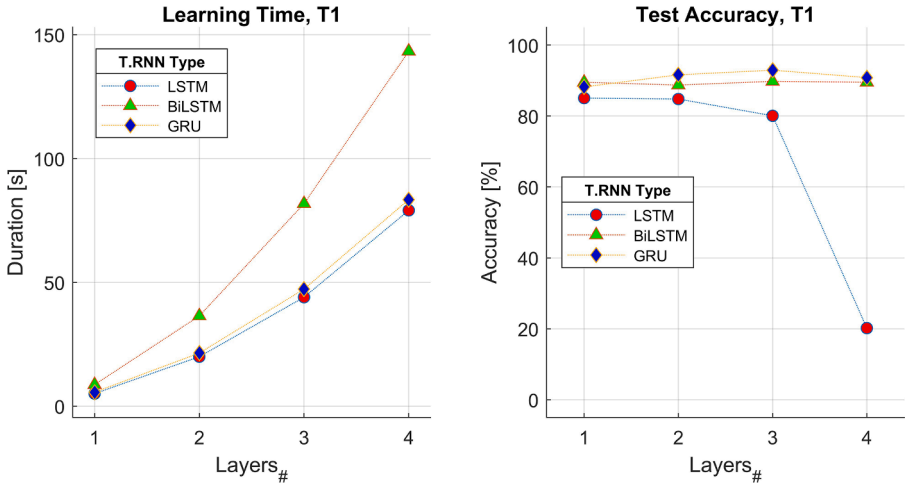

Fig. 40. Learning time (Left) and test accuracy (Right) of sector collisions for different T1 RNN types; increasing taught layers minimally affects BiLSTM and GRU, while LSTM's accuracy declines. Learning time is reduced by 30 % compared to T0.

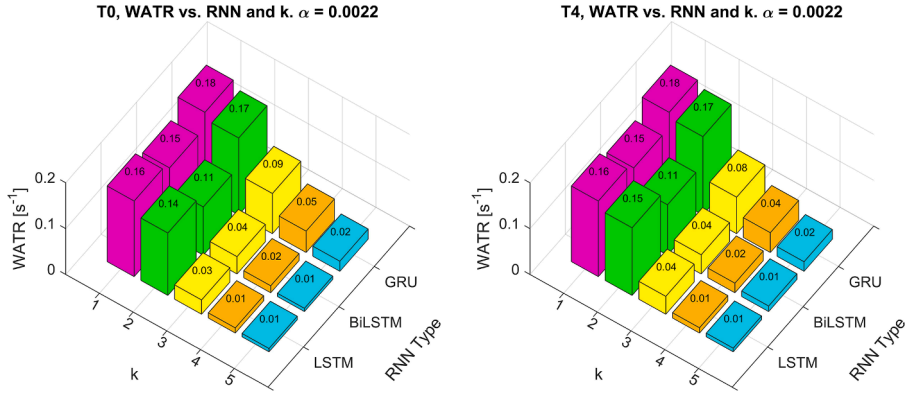

Fig. 41. WATR for T0 (Left) and T4 (Right) homogeneous RNN types; GRU outperforms other NN types for both T0 and T4, while there is a slight difference between one and two layers, the higher testing accuracy is achieved with two layers, despite the increased learning time.

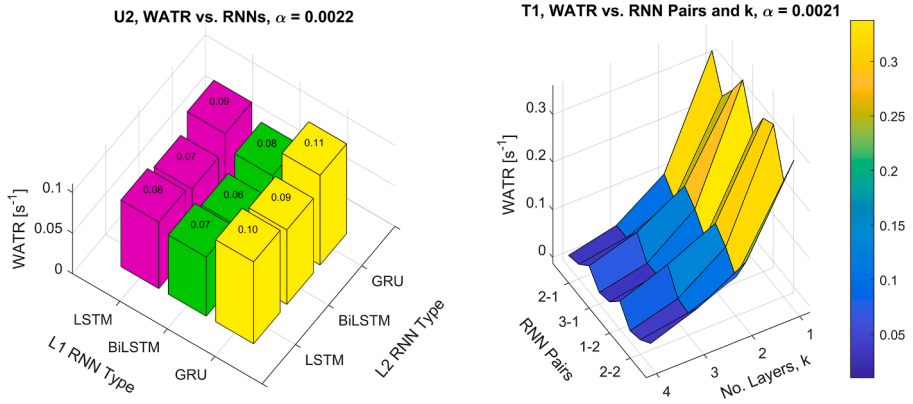

Fig. 42. WATR for U2 (Left) and T1 (Right) heterogeneous RNN types; for U2 GR layers provide the best performance, while for T, increasing taught layers decreases the WATR value.

efficiency of the suggested neural network model.

In future work, we will explore the different configurations of RNN layers to gain deeper insights into the effectiveness of the TL techniques across various patterns. These additional experiments aim to uncover potential improvements and fine-tune the approach for better performance.

4.4. Feature analysis with generative AI

Generative AI, particularly GANs has gained prominence for its capability in creating realistic synthetic data and models by training neural networks in a competitive setup. In the next cellular networks, generative AI promises to generate more realistic a significant synthetic network data and simulate complex scenarios. Generating realistic synthetic data is widely used for training machine learning models where large, labeled data sets are essential but hard to obtain due to various limitations [44]. And because 6G is still now in the theoretical and simulation phase, synthetic data may provide an essential resource for testing and developing models under realistic conditions without needing physical infrastructure. Due to the complexity of the ADAPT system, simulating for just 10 *ms* incurs a significant computational load, especially for larger population densities. This short simulation period is not enough to capture the full system behavior, especially under varied network loads. To address this, we aim to analyze whether GAN methods can generate high-fidelity synthetic data that accurately represents the complex behavior within the ADAPT system. Evaluating the performance of these applied GAN methods will involve using some similarity metrics to determine the performance of the generated synthetic data compared to the real one. This will help us to improve our understanding of the methods used and enable enhancements in efficiency and adaptability.

4.4.1. Feature analysis

Generative AI uses various models and techniques for generating text, images, audio, and other types of data to create a new data set that resembles existing patterns. Generative Adversarial Networks (GAN) AI comprises two main neural networks; the generator and the discriminator, each has a different and important role for generating similar data. The generator neural network generates data from random noise while the discriminator aims to differentiate between genuine data from the original dataset and the synthetic data generated by the generator, this aspect is represented in the Fig. 43.

GAN has transformed the field of data generation and augmentation. Integration of this approach with the 6G wireless networks could significantly improve the performance of data augmentation, making it more representative of the real world [45]. We choose to use GAN and 4 from its method types (Adversarial Autoencoder (AAE), Deep Convolutional GAN (DCGAN), Least Squares GAN (LSGAN), Wasserstein GAN (WGAN)) explained in Table 6 to generate synthetic data to the Shannon entropy metrics M and R, to see the behavior of these types and compare in between.

We decided to start first with these well-known GAN methods to see their performance on our data sets and decide how to improve the existing algorithms based on the quality of the results obtained. With every GAN method, we generate twenty synthetic pairs M and R having a total of 1400 per GAN method (having 20 from $n \in$ V, where set V is the number of MTs, $V = \{15,\ 30,\ 60,\ 120,\ 240,\ 480,\ 960\}$, $d \in \{\mathrm{d1},\ \mathrm{d2}\}$ and the overlapping ratio $m \in \{0.1,\ 0.3,\ 0.5,\ 0.7,\ 0.9\}$).

However, an important consideration is assessing the degree of similarity between the original par $\{M, R\}$ and the generated using GAN methods. To achieve this, different similarity metrics may be employed to quantify the effectiveness of the used GAN type. This leads us to select six well-known metrics to gauge how closely the generated pair $\{M, R\}$ matched the original pair data sets, this can provide insights into the reliability of the outputs. The chosen similarity metrics for this evaluation are shown in the Table 7, includes: Correlation similarity, Cosine similarity, Dynamic Time Warping (DTW), Fréchet Inception Distance (FID), Peak Signal-to-Noise Ratio (PSNR), and Root Mean Square Error (RMSE). The correlation and cosine similarity has proven its usability in evaluating linear relations and angular similarities as it was mentioned in the study referenced in [46]. Therefore, we got inspired to evaluate the GAN methods' similarity using it.

Moreover, DTW is particularly useful for measuring similarities between time-series data, DTW was used as a classification method for time series in [47], while it was studied and examined as a similarity metric in [48], using FID, they found that is useful for measuring the quality of generated images and the diversity of synthetic data, providing a better view of how closely the synthetic data approximates the real distribution. We got inspired from a similar work [49] where the researchers talked about the use of it to evaluate the GAN method, using PSNR and RMSE to quantify the reconstruction error and fidelity of the synthetic data, ensuring that the outputs maintain high accuracy compared to the original one. Table 7 lists the formula of the similarity metric used for evaluating the GAN methods' performance. A scatter plot and 3D histogram of the resulting testing evaluations of the generated Shannon entropy

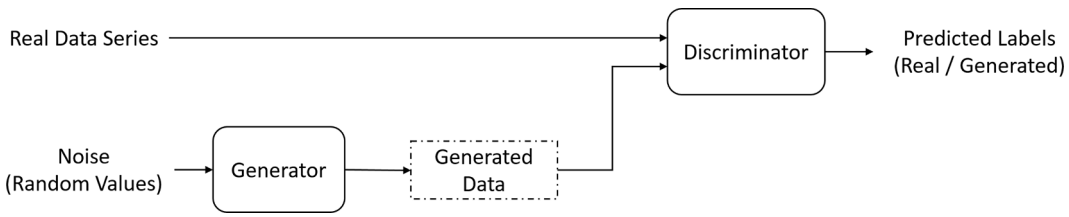

Fig. 43. Architecture of the GAN system.

Table 6
List of GAN methods.

	Generative AI method	Internal Layers
1.	AAE	**Encoder:** convolution layers/dense layers, batch normalization, and activation functions (ReLU). **Decoder:** transposed convolution layers/dense layers to reconstruct the input data. **Discriminator:** convolution/dense layers.
2.	DCGAN	**Generator:** Transposed convolution layers, batch normalization, and ReLU activations **Discriminator:** Convolution layers, batch normalization, and Leaky ReLU activations.
3.	GAN	**Generator:** fully connected layers, transposed convolution layers **Discriminator:** convolution layers and dense layers to classify real or fake.
4.	LSGAN	**Generator:** Dense layer, transposed convolution layers, batch normalization, and ReLU activation. **Discriminator:** Convolution layers, Leaky ReLU, and dense layers.
5.	WGAN	**Generator:** Dense layer, batch normalization, ReLU activation, and transposed convolutional layer with Tanh activation. **Discriminator:** Convolutional layers, leaky ReLU activation, and dense layers.

Table 7
List of similarity metrics.

Metric	Formula
CORR	$CORR(x,y) = \frac{\sum_{i=1}^{n}(x[i]-\bar{x})(y[i]-\bar{y})}{\sqrt{\sum_{i=1}^{n}(x[i]-\bar{x})^2\sum_{i=1}^{n}(y[i]-\bar{y})^2}}$
COS	$COSI(x,y) = \frac{\sum_{i=1}^{n}x[i]y[i]}{\sqrt{\left(\sum_{i=1}^{n}x[i]^2\right)\left(\sum_{i=1}^{n}y[i]^2\right)}}$
DTW	$D[1,1] = dist(x[1],y[1])$ *% Initialize Cost Matrix* **for** i = 1:n1 **for** j = i:n2 $dist(x[i],y[j]) = (x[i]-y(j))^2$ *% Euclidean distance* $D[i,j] = dist(x[i],y[j]) + min\begin{cases} D[i-1,j] \\ D[i,j-1] \\ D[i-1,j-1] \end{cases}$ $DTW(x,y) = D[n1,n2]$ *% Ḋ is bottom-right cell of the D*
FID	$COV(x),\ COV(y)$ *% Covariance of x and y* $FID(x,y) = (\bar{x}-\bar{y})^2 + Trace\left(\left(\sqrt{COV(x)} - \sqrt{COV(y)}\right)^2\right)$
PSNR	$MSE(x,y) = \frac{1}{n}\sum_{i=1}^{n}(x[i]-y[i])^2$ *% Mean Squared Error* $\max(x)$ *% Maximum of x* $PSNR(x,y) = 20log_{10}(\max(x)) - 10log_{10}(MSE(x,y))$
RMSE	$RMSE(x,y) = \sqrt{\frac{1}{n}\sum_{i=1}^{n}(x[i]-y[i])^2}$

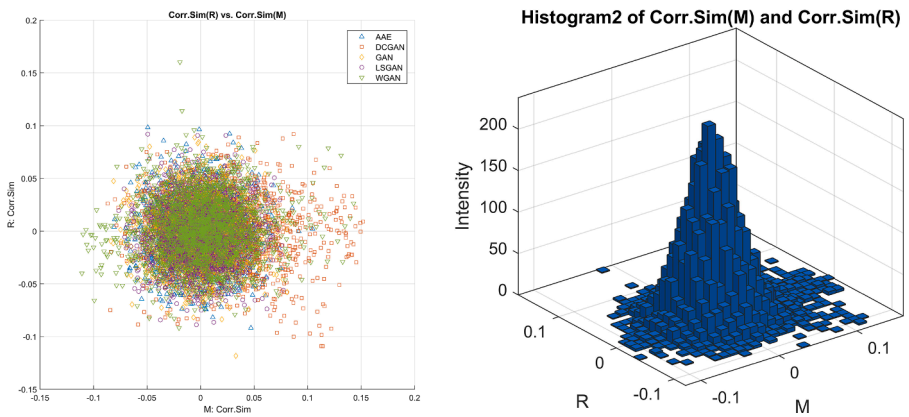

Fig. 44. Correlation similarity, Scatter plot (Left); shows no correlation between the original and GAN-generated data. 3D histogram (Right) of the pair {*M, R*} reveals a high concentration at the center having limited correlation detection.

metrics pair {*M, R*} using the mentioned similarity metrics are plotted in the figures that are explained and discussed in the next subsection, each plot contains all the generated 70 cases twenty times ($70 \times 20 = 1400$) using all 5 GAN types.

4.4.2. Results and discussion

We analyze the evaluations of the generated Shannon entropy metrics {*M, R*} through various visual representations, including scatter plots and 3D histograms. The following discussion will focus on interpreting the results and their significance for future research and applications.

The correlation similarity between the original Shannon entropy metric pair and the generated ones using all the GAN methods shows no similarity in between (concentrated around 0) meaning zero correlating in between and this is seen in Fig. 44 (Left). The 3D histogram shows the high concentration of the boxes in the center of Fig. 44 (Right). This finding could present the limitation of correlation similarity in detecting the similarity level between the synthetic and real data. Correlation metric only captures linear relationships and may miss non-linear dependencies, which are important in understanding complex data behavior. One must note that the correlation metric is sensitive to outliers that can destroy the results, leading to an incomplete representation of the similarity between the original and generated datasets.

Evaluating the similarity using cosine shows dispersed dots ranging from -1 to 1, cosine being -1 means that the data sets are opposed, while cosine 0 indicates that the vectors are orthogonal to each other and not similar and cosine 1 illustrates that the generated synthetic data are identical with the real data set (Fig. 45 (Left)). While the 3D histogram shows the dense boxes around 0 cosine (Fig. 45 (Right)).

This diversity could provide a more sophisticated perspective on how the vectors relate to one another. The cosine similarity metric focuses on the orientation of the vectors and ignores their magnitudes. Therefore, two datasets with similar directions but differing scales could result in a high cosine similarity score. This limitation masks the essential differences in their distribution and overall characteristics.

Dynamic time warping illustrates how all the 5 GAN methods generate different data sets from a similar point of view with different intensities (see Fig. 46 (Right)). Fig.46 (left) shows that the yellow diamonds (GAN) dispersed far from each other being wrong, meanwhile, the red squares (DCGAN) performed better than the others. The good performance of the DCGAN indicated by its closer clustering, may imply that it captures the underlying structure of the data more effectively compared to other GAN methods.

DCGAN proves its high performance with frechet inception distance as well, having lower values, this finding suggests that DCGAN excels in generating high-fidelity synthetic data. Conversely, the traditional GAN method has a bad generation with high FID values (see Fig. 47 (Left)). The intensive boxes in the lower corner represent the rest of the GAN types: AAE, LSGAN, and WGAN, where they show comparable performances (Fig. 47 (Right)), which indicates that they might generate more realistic synthetic data than the traditional GAN but still not reach the performance level of DCGAN. Furthermore, we can say that the FID metric could capture the similarity level of the synthetic data and could cluster the applied GAN methods based on their performances.

One has to notice, a high PSNR indicates the high performance of the used method. Hence, The GAN method clustered lower than the rest with poor quality, DCGAN shows the best performance, approximately 20 for the metric R and around 8 for the metric M producing a high-quality of generated dataset (Fig. 48 (Left)), while the rest of the GAN methods clustered closer to each other, and this is clear in the 3D histogram (Fig. 48 (Right)). PSNR highlighted the superiority of DCGAN in generating synthetic data with better fidelity.

While it clusters the rest of the GAN methods close to each other, it indicates that they might share similar limitations in data quality, which could affect their applicability in critical use cases.

Nevertheless, Similar findings were observed when calculating the RMSE metric for the synthetic and the original Shannon entropy metric pair {*M, R*} using the five different methods. For DCGAN, the metric R was closer to 0 having minimal error, while metric M ranged between 0.4 and 1, still indicating relatively good performance (Fig. 49 Left). In contrast, the standard GAN method Exhibited

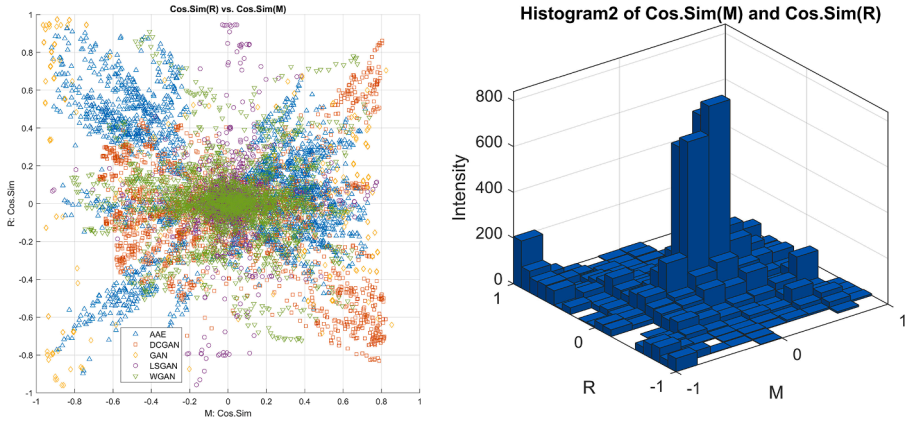

Fig. 45. Cosine Similarity, Scatter plot (Left) shows cosine values ranging from -1 to 1, indicating varying similarity. And 3D histogram (Right) of the pair {*M, R*} reveals dense clustering around cosine 0, suggesting diversity in vector relationships.

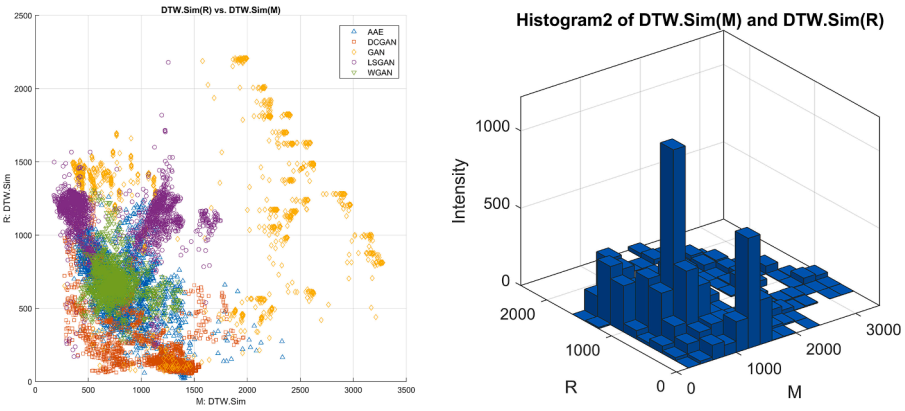

Fig. 46. DTW, Scatter plot (Left) highlighting the good performance of DCGAN (red squares) and 3D histogram (Right) of the pair {*M, R*} highlights varying intensities in data generation.

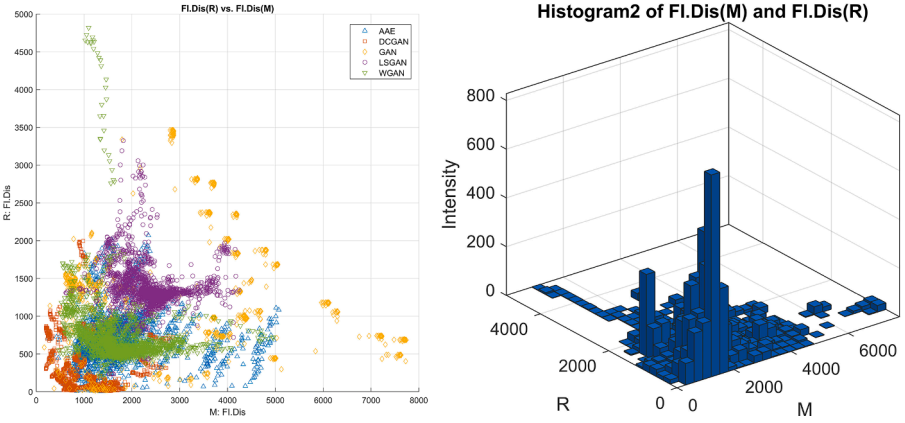

Fig. 47. FID, Scatter plot (Left) shows DCGAN excels with lower FID values, indicating high-fidelity data generation, and 3D histogram (Right) of the pair {*M, R*}shows AAE, LSGAN, and WGAN perform similarly.

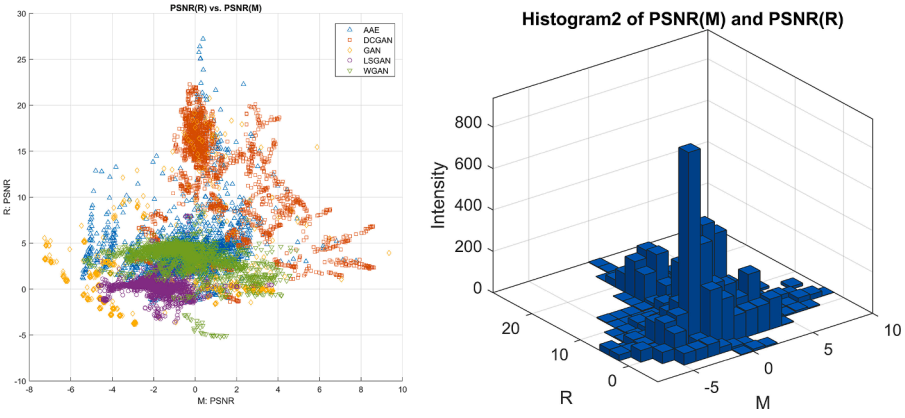

Fig. 48. PSNR, Scatter plot (Left) shows DCGAN outperforms others with the highest PSNR, and 3D histogram (Right) of the pair {*M, R*} reveals the clustering of other GAN methods, which perform similarly but lower than DSGAN.

an RMSE closer to 2 reflecting higher errors and lower data quality compared to the other used methods. 3d histogram in Fig. 49 Right shows a high intensity concentrated around 1 representing the comparable dataset produced by the three GAN types" AAE, LSGAN, and WGAN.

OPTICS (Ordering Points To Identify the Clustering Structure) is a density-based clustering algorithm, it is designed to identify

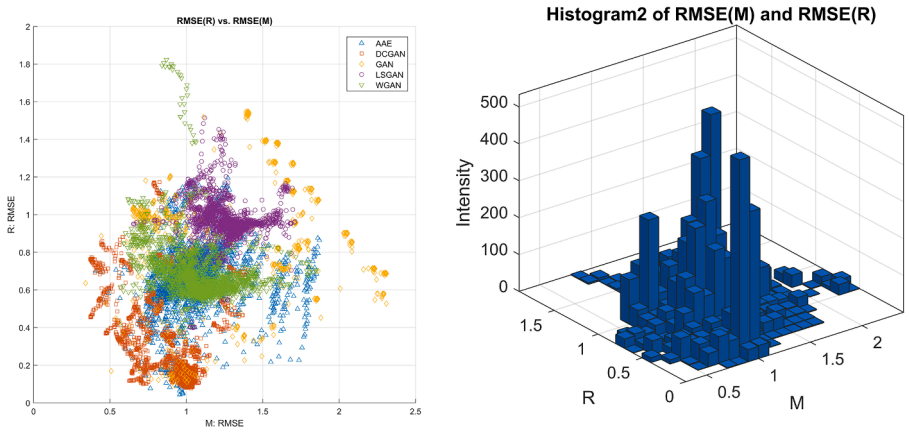

Fig. 49. RMSE, Scatter plot (Left) shows DCGAN with minimal RMSE, and 3D histogram (Right) of the pair $\{M, R\}$ displays a high intensity around RMSE $= 1$ for AAE, LSGAN and WGAN, showing comparable performance among these methods.

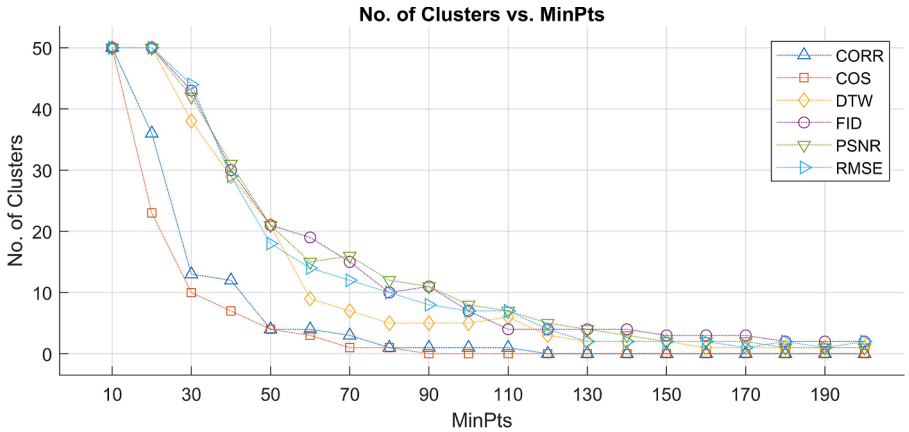

Fig. 50. Dependence of the number of the clusters on the parameter MinPts of the OPTICS, exponential decay in cluster counts relative to MinPts, with six similarity metrics grouped by clustering behavior.

clusters of varying densities and shapes by creating an ordering of the data points based on their reachability distances. While it forms a dense region or cluster based on the MinPts parameter (refers to the minimum number of points within a cluster). By using the OPTICS algorithm, we aim to compare the similarity metrics used in evaluating the GAN Methods. The analysis revealed an exponential decay relationship between the number of clusters and the minimum number of points required to form a cluster as illustrated in the Fig. 50. Notable, the six-similarity metrics demonstrated distinct results in this context. These metrics are categorized into three main groups based on their clustering characteristics relative to the MinPts:

Group 1: {FID, PSNR, RMSE},

Table 8
Comparison of the used metrics for generative AI.

Metric Name	Feature Capture	Evaluation	Cost/Complexity
Cosine Similarity	(-)	Poor at capturing subtle differences and temporal patterns.	Low computational cost.
Correlation Similarity	(-)	Fails to capture non-linear relationships or temporal variations.	Low computational cost.
Dynamic Time Warping	(+)	Excellent for capturing similarity levels, aligning sequences even if they are out of sync.	High computational cost.
Fréchet Inception Distance	(+)	Effective for feature selection, captures relevant features based on their importance.	Moderate to high computational cost.
Pick Signal to Time Ratio	(+)	Common in image processing, captures feature similarity by comparing signal quality.	Low to moderate computational cost.
Root Mean Square Error	(+)	Captures errors, good for regression tasks where small differences matter.	Low computational cost.

Group 2: {DTW},
Group 3: {CORR, COS}.

The DTW metric exhibited a medium number of clusters compared to others within the MinPts parameter range of {60, 70, …,100}. These findings emphasize the importance of selecting the appropriate similarity metrics for effective analysis of complex data structures, as it could easily evaluate the performance of the method used in the wrong way.

Evaluating the similarity level between the original Shannon entropy metric pair {*M, R*} and the generated ones using various similarity metrics across five generative AI types (AAE, DCGAN, GAN, LSGAN, and WGAN), it was evident that the GAN type called DCGAN outperformed the others, proving superior synthetic data quality and better alignment with the original data. On the other hand, the traditional GAN type showed the worst performance among all methods, indicating lower quality and higher error rates. These findings highlight the importance of selecting the appropriate GAN model for specific applications. Moreover, the evaluation results proved the limitations of both correlation and cosine similarities (see Table 8, Fig. 50) in capturing the resemblance and quantifying the similarity level between the original entropy pair {*M, R*} vectors and the generated vectors in contrast to other used similarity metrics (DTW, FID, PSNR, and RMSE).

The synthetic data generated by the GANs can present both risks and opportunities for the next cellular communication generation and future technology. One major concern is the vulnerability of data generated to manipulations, if happen that the attackers could access or influence the GAN model, then it is easy for them to introduce subtle biases or inaccuracies that affect the reliability and security of network applications. The inherent limitations of the GANs in capturing highly complex or rare patterns might lead to data inaccuracies and lower model performance in real-world scenarios. Also, generative AI methods demand high computational power while its training process is often unstable, making it unsuitable for high-stakes applications. Nevertheless, we cannot deny that the synthetic data carries some privacy risks, like unintentional retention and recreation of some sensitive patterns from the original datasets leading to exposing sensitive information. Especially where high-fidelity, individual-like synthetic data is generated, making it possible to trace back to real-world users. Meanwhile, some strategies can be employed where the privacy of the user is a priority, like *differential privacy* [50] techniques, where white noise is added to the original data to reduce the recreation of sensitive information. Also, *privacy-preserving machine learning* [51] methods like federated learning can be leveraged, allowing the GAN model to learn from the distributed data source without getting close to the sensitive information. Other strategies are used in practice to keep the user's privacy while enabling GANs to generate valuable synthetic data. Generative AI remains a potential way for generating large, realistic datasets that can augment the limited real-world data, enhance model robustness, and facilitate simulations for scenarios that are challenging to replicate in real-world conditions. These benefits highlight GANs' value for the 6G, though careful management of their limitations and security risks is essential for safe and effective applications.

4.5. AI-driven insights and usability of 6G applications

The practical implications of this research are significant for advancing the development and deployment of 6G networks. The methods and insights presented provide a roadmap for addressing key challenges in the future real-world applications, offering innovative solutions to enhance network performance, reliability, and adaptability. In scenarios characterized by dynamic and high-density environments, such as urban centers or industrial IoT deployments, the ability to process complex and time-sensitive data is critical. This research supports these demands by highlighting efficient methodologies for feature extraction (findings of *subsection 4.1*.), clustering (findings of *subsection 4.2*.), and predictive modeling (findings of *subsection 4.3*.). The proposed approaches can streamline processes such as dynamic resource allocation, anomaly detection, and collision management, enabling networks to maintain high performance even under challenging conditions.

For practical deployment, the findings suggest the importance of adaptive algorithms capable of real-time adjustments to varying network states. By incorporating robust clustering methods (findings of *subsection 4.2*.) and predictive modeling techniques (findings of *subsection 4.3*.), network operators can optimize efficiency while minimizing computational overhead. Additionally, the generation of synthetic data (findings of *subsection 4.4*.) provides an invaluable tool for testing and validating network protocols in scenarios where real-world data is limited or unavailable. This capability is crucial for simulating extreme conditions or novel use cases, ensuring the reliability of solutions before they are deployed.

The reliability and applicability of synthetic data have been reinforced through theoretical validation, which is considered a robust approach. However, stronger validation would involve aligning synthetic data with real-world benchmarks. This can only be achieved once 6G devices become available on the market. Strategies such as these 'coupled with advanced metrics tailored to specific network scenarios ensure that synthetic data accurately reflects the complexities of real-world conditions, thus enhancing its applicability in supporting innovative applications for 6G networks.

To ensure the broader applicability and security of these methods, attention must be given to potential risks, such as privacy concerns and vulnerability to adversarial attacks. Employing privacy-preserving techniques, such as federated learning or differential privacy, can safeguard sensitive information while maintaining the utility of generated data. Moreover, integrating these methods into practical 6G architecture will require collaboration across disciplines to address hardware constraints, interoperability, and scalability. The findings of this study provide a foundation for future innovations in 6G technology. They highlight pathways for optimizing network operations, ensuring scalability, and supporting diverse applications, from smart cities to autonomous systems. By bridging theoretical advancements with practical implementation strategies, this work contributes to a more actionable framework for the next-generation wireless communication networks.

5. Conclusion

Studying the new MAC mechanism ADAPT from different aspects helps in understanding more the behavior of the protocol which leads to enhancing the new technology. Transmission distances, collision rate, throughput, and received power, all properties were taken into consideration in the analysis while different simulation scenarios were executed in addition to the dual parameters: rotation step and overlapping ratio that played a crucial role in the ADAPT system. Applying a powerful mathematical tool like Shannon entropy contributed to the enhancement of technology, where we evaluated the mutual effect between the two different subsystems introducing usable metrics for characterizing the transmission power of the MTs in ADAPT. Shannon entropy metrics reveal the interactions between subsystems in the THz MAC mechanism, emphasizing their impact on communication performance. Moreover, the use of wavelet transform proves its capability in feature extraction with an accurate result of the RNN model in a super short time, approximately 47 seconds, and even DBScan-based unsupervised learning proves its competence in categorizing different classes. In addition to that, the proposed metric WATR could successfully quantify the goodness of the transfer learning multi-layer RNN models by considering both the accuracy and learning time. Other transfer learning models can be studied and applied in the next study stage in order to discover other unknown behaviors. As for the fourth AI method, we applied five different generative AI methods where twenty synthetic data were produced per method. By calculating the similarity using 6 similarity metrics, it was validated that DCGAN had the highest performance. These results indicate testing the labeled GAN in future work and integrating other types of neural networks (convolutional, transformer, etc.) would be interesting and helpful. Higher order flux of the entropy will be analyzed in the continuation of this research.

These findings outline the significance of the PACP method in enhancing the performance of communication systems. By combining classical mathematical tools with AI techniques, PACP not only optimizes data processing but also improves feature extraction, leading to more accurate models. This contribution is pivotal for advancing the capabilities of the next wireless communication generation, particularly THz-based networks, where efficient resource allocation and robust communication strategies are essential for meeting the demands of future applications. Nevertheless, PACP simplifies the complexity of data while also reducing costs, making it a viable solution for future technology. The current study is analyzing events in micro timescales, therefore future research will focus on extending the scope of our analysis by evaluating events over a macro timescale, specifically within the range of 10 to 60 seconds. This broader temporal perspective will provide a more comprehensive understanding of the overall MAC system. In the next research phase, we plan also to enhance the ADAPT protocol to simulate both uplink and downlink communications, rather than being limited to uplink only. The extension will allow us to explore the full potential of the communication system. Furthermore, we aim to incorporate additional classical mathematical processing tools for enhancing and extracting features for assessing their impact on AI performance, thereby refining our approach to the accuracy of our results. This multi-faceted research agenda will contribute to the development of more efficient and adaptable communication strategies for the upcoming generation of wireless networks.

CRediT authorship contribution statement

Djamila Talbi: Writing – review & editing, Writing – original draft, Visualization, Validation, Resources, Methodology, Formal analysis, Data curation. **Zoltan Gal:** Writing – review & editing, Writing – original draft, Validation, Supervision, Software, Project administration, Methodology, Formal analysis, Data curation, Conceptualization.

Declaration of competing interest

The authors declare that they have no known competing financial interests or personal relationships that could have appeared to influence the work reported in this paper.

Acknowledgments

This work has been supported by the QoS-HPC-IoT Laboratory and project TKP2021-NKTA of the University of Debrecen, Hungary. Project no. TKP2021-NKTA-34 has been implemented with the support provided by the Ministry of Culture and Innovation of Hungary from the National Research, Development and Innovation Fund, financed under the TKP2021-NKTA funding scheme. Another supporting project was OMAA 116öu7 of the Austro-Hungarian Action Foundation.

Data availability

Data will be made available on request.

References

[1] T. Taleb, R. Aguiar, G. Luis, I. Ben Yahia, et al., White paper on 6G networking, in: S. Ali, W. Saad, D. Steinbach (Eds.), White Paper on Machine Learning in 6G Wireless Communication Networks, 2020. White paper. *6G Research Visions*, No.7, June 2020.

[2] Q. Xia, Z. Hossain, M. Medley, et al., A link-layer synchronization and medium access control protocol for terahertz-band communication networks, IEEE Trans. Mob. Comput. 20 (1) (2019) 2–18.

[3] I.F. Akyildiz, J.M. Jornet, C. Han, Terahertz band: next frontier for wireless communications, Phys. Commun. 12 (2014) 16–32.

[4] S. Koenig, D. Lopez-Diaz, J. Antes, et al., Wireless sub-THz communication system with high data rate, Nat. Photonics. 7 (12) (2013) 977–981.
[5] K. Suresh, A. Alqahtani, T. Rajasekaran, et al., Enhanced metaheuristic algorithm-based load balancing in a 5G cloud radio access network, Electronics. (Basel) 11 (21) (2022) 3611.
[6] Han, C., Wu, Y., Chen, Z., et al. Terahertz communications (TeraCom): challenges and impact on 6G wireless systems. *arXiv preprint arXiv:1912.06040*, 2019.
[7] S. Ghafoor, N. Boujnah, M.H. Rehmani, et al., MAC protocols for terahertz communication: a comprehensive survey, IEEE Commun. Surv. Tutor. 22 (4) (2020) 2236–2282.
[8] W.S. Jiang, D. Hans, Full-spectrum wireless communications for 6G and beyond: from microwave, millimeter-wave, terahertz to lightwave, in: 2023 IEEE 3rd International Conference on Computer Communication and Artificial Intelligence (CCAI), IEEE, 2023, pp. 353–357.
[9] W. Osamy, A. Salim, A.M. Khedr, An information entropy based-clustering algorithm for heterogeneous wireless sensor networks, Wirel. Netw. 26 (2020) 1869–1886.
[10] C. Carvalho, E. Mota, E. Ferraz, et al., Entropy based routing for mobile, low power and lossy wireless sensors networks, Int. J. Distrib. Sens. Netw. 15 (7) (2019) 1550147719866134.
[11] J. Zhang, Z. Lin, P.-W. Tsai, et al., Entropy-driven data aggregation method for energy-efficient wireless sensor networks, Inf. Fusion. 56 (2020) 103–113.
[12] L. Li, J. Wang, Research on feature importance evaluation of wireless signal recognition based on decision tree algorithm in cognitive computing, Cogn. Syst. Res. 52 (2018) 882–890.
[13] Z.L. Wang, Entropy theory of distributed energy for internet of things, Nano. Energy. 58 (2019) 669–672.
[14] M. Gabrié, A. Manoel, C. Luneau, et al., Entropy and mutual information in models of deep neural networks, Adv. Neural Inf. Process. Syst. 31 (2018).
[15] M. Ceci, R. Corizzo, D. Malerba, et al., Spatial autocorrelation and entropy for renewable energy forecasting, Data Min. Knowl. Discov. 33 (3) (2019) 698–729.
[16] Y.M. Omar, P. Plapper, A survey of information entropy metrics for complex networks, Entropy. 22 (12) (2020) 1417.
[17] L.-L.K. Xie, R. Panganamala, A network information theory for wireless communication: scaling laws and optimal operation, in: IEEE Trans. Inf. Theory., 50, 2004, pp. 748–767.
[18] J.P.S Coon, J. Peter, Topological entropy in wireless networks subject to composite fading, in: 2017 IEEE International Conference on Communications (ICC), IEEE, 2017, pp. 1–7.
[19] A. Ali, S. Anam, M.M. AHMED, Shannon entropy in artificial intelligence and its applications based on information theory, J. Appl. Emerg. Sci. 13 (1) (2023) 09–17.
[20] C.O. Sakar, S.O. Polat, M. Katircioglu, et al., Real-time prediction of online shoppers' purchasing intention using multilayer perceptron and LSTM recurrent neural networks, Neural Comput. Appl. 31 (2019) 6893–6908.
[21] T. Ren, X. Liu, J. Niu, X. Lei, Z. Zhang, Real-time water level prediction of cascaded channels based on multilayer perception and recurrent neural network, J. Hydrol. (Amst) 585 (2020).
[22] K. Ali, S. Khan, A. Ahmad, A. Ur Rehman, et al., Learned-SBL-GAMP based hybrid precoders/combiners in millimeter wave massive MIMO systems, PLoS. One. 18 (9) (2023) e0289868.
[23] M.K Hasan, M.TE. Elahi, M.A. Alam, M.T Jawad, R. Martí, Dermoexpert: skin lesion classification using a hybrid convolutional neural network through segmentation, transfer learning, and augmentation, Inform. Med. Unlocked. 28 (2022).
[24] D. Jozinović, A. Lomax, I. Štajduhar, A. Michelini, Transfer learning: improving neural network-based prediction of earthquake ground shaking for an area with insufficient training data, Geophys. J. Int. 229 (1) (2022). April.
[25] S. Kolagati, T. Priyadharshini, V. Mary Anita Rajam, Exposing deepfakes using a deep multilayer perceptron – convolutional neural network model, Int. J. Inf. Manag. Data Insights. 2 (2022).
[26] A. Pimpalkar, et al., MBiLSTMGloVe: embedding GloVe knowledge into the corpus using multi-layer BiLSTM deep learning model for social media sentiment analysis, Expert. Syst. Appl. 203 (2022) 117581.
[27] P. Uthansakul, P. Anchuen, M. Uthansakul, et al., Estimating and synthesizing QoE based on QoS measurement for improving multimedia services on cellular networks using ANN method, IEEE Trans. Netw. Serv. Manag. 17 (1) (2019) 389–402.
[28] P. Uthansakul, P. Anchuen, M. Uthansakul, et al., QoE-aware self-tuning of service priority factor for resource allocation optimization in LTE networks, IEEE Trans. Veh. Technol. 69 (1) (2019) 887–900.
[29] C. Coleman, D. Kang, D. Narayanan, et al., Analysis of dawnbench, a time-to-accuracy machine learning performance benchmark, ACM SIGOPS Oper. Syst. Rev. 53 (1) (2019) 14–25.
[30] A.F. Psaros, X. Meng, Z. Zou, et al., Uncertainty quantification in scientific machine learning: methods, metrics, and comparisons, J. Comput. Phys. 477 (2023) 111902.
[31] K. Lakshmanna, R. Kaluri, N. Gundluru, et al., A review on deep learning techniques for IoT data, Electronics. (Basel) 11 (10) (2022) 1604.
[32] D.&. Morales, J. Jornet, ADAPT: an adaptive directional antenna protocol for medium access control in terahertz communication networks, Ad. Hoc. Netw. 119 (2021). Mai.
[33] V. Petrov, T. Kurner, I. Hosako, IEEE 802.15.3d: first standardization efforts for sub-terahertz band communications toward 6G, IEEE Commun. Mag. 58 (11) (2020) 28–33. November.
[34] Z. Hossain, Q. Xia, J.M. Jornet, TeraSim: an ns-3 extension to simulate terahertz-band communication networks, Nano Commun. Netw. 17 (2018) 36–44. September.
[35] S. Sahoo, B. Kanungo, S. Behera, et al., Multiresolution wavelet transform based feature extraction and ECG classification to detect cardiac abnormalities, Measure. 108 (2017) 55–66.
[36] T.M. Cover, JA. Thomas, Entropy, relative entropy and mutual information, Element. Inf. Theory. 2 (1) (1991) 12–13.
[37] et T. Tuncer, S. Dogan, A. Subasi, Surface EMG signal classification using ternary pattern and discrete wavelet transform based feature extraction for hand movement recognition, Biomed. Signal. Process. Control. 58 (2020) 101872.
[38] Y. Wang, X. Du, Z. Lu, et al., Improved LSTM-based time-series anomaly detection in rail transit operation environments, IEEE Trans. Industr. Inform. 18 (12) (2022) 9027–9036.
[39] O. Aouedi, K. Piamrat, S. Hamma, et al., Network traffic analysis using machine learning: an unsupervised approach to understand and slice your network, Ann. Telecommun. 77 (5) (2022) 297–309.
[40] J.S. Alrubaye, B. Shahgholi Ghahfarokhi, Resource-aware DBSCAN-based re-clustering in hybrid C-V2X/DSRC vehicular networks, PLoS. One. 18 (10) (2023) e0293662.
[41] F. Zhuang, Z. Qi, K. Duan, et al., A comprehensive survey on transfer learning, in: Proceedings of the IEEE 109, 2020, pp. 43–76.
[42] I. Ameer, N. Bölücü, M.H.F. Siddiqui, et al., Multi-label emotion classification in texts using transfer learning, Expert. Syst. Appl. 213 (2023) 118534.
[43] H. Lu, J. Wu, Y. Ruan, et al., A multi-source transfer learning model based on LSTM and domain adaptation for building energy prediction, Int. J. Electr. Power Energy Syst. 149 (2023) 109024.
[44] A. Karapantelakis, P. Alizadeh, A. Alabassi, et al., Generative AI in mobile networks: a survey, Ann. Telecommun. 79 (1) (2024) 15–33.
[45] Z. Tao, W. Xu, Y. Huang, et al., Wireless Network Digital Twin For 6G: generative AI as a Key Enabler, 31, IEEE Wireless Communications, 2024, pp. 24–31.
[46] H.D. Satea, A.A. Ibrahem, M. Faiq, et al., Similarity measurement's comparison with mapping and localization in large-scale, in: AIP Conference Proceedings, AIP Publishing, 2023.
[47] P. Senin, Dynamic Time Warping Algorithm Review 855 (1-23) (2008) 40.
[48] L.F. Buzuti, C.E. Thomaz, Fréchet AutoEncoder distance: a new approach for evaluation of generative adversarial networks, Comput. Vis. Image Underst. 235 (2023) 103768.

[49] U. Sara, M. Akter, U. Et, M. Shorif, Image quality assessment through FSIM, SSIM, MSE and PSNR—a comparative study, J. Comput. Commun. 7 (3) (2019) 8–18.
[50] M. Yang, T. Guo, T. Zhu, et al., Local differential privacy and its applications: a comprehensive survey, Comput. Stand. Interfaces. (2023) 103827.
[51] Xu, R., Baracaldo, N., et Joshi, J. Privacy-preserving machine learning: methods, challenges and directions. *arXiv preprint arXiv:2108.04417*, 2021.